External Award 04HQGR0035

Program Element III
Panel EP

INFLUENCE OF DIGITAL ELEVATION MODEL ERRORS ON THE RELIABILITY OF MAPS DEPICTING EARTHQUAKE-TRIGGERED LANDSLIDE HAZARDS

Principal Investigator:

William C. Haneberg

Haneberg Geoscience, 10202 39th Avenue SW, Seattle WA 98146

(206) 935-0846
bill@haneberg.com

Research supported by the U.S. Geological Survey (USGS), Department of the Interior, under USGS award number 04HQGR0035. The views and conclusions contained in this document are those of the author and should not be interpreted as necessarily representing the official policies, either expressed or implied, of the U.S. Government.

Haneberg
Geo•science

CONTENTS

TECHNICAL ABSTRACT

External Award 04HQGR0035

INFLUENCE OF DIGITAL ELEVATION MODEL ERRORS ON THE RELIABILITY OF MAPS DEPICTING EARTHQUAKE-TRIGGERED LANDSLIDE HAZARDS

William C. Haneberg
Haneberg Geoscience, 10202 39th Avenue SW, Seattle WA 98146, (206) 935-0846,
bill@haneberg.com

More than 1700 centimeter accurate differential global positioning system (GPS) measurements were used to estimate elevation errors in a conventional USGS 10 m digital elevation model (DEM) and a 1 m light detection and ranging (LiDAR) DEM covering an 18 km^2 portion of Seattle, Washington. Elevation errors were estimated by importing the GPS data into a 1 m raster grid and subtracting the DEM elevations. The 10 m DEM errors had a declustered mean of –0.92 m and standard deviation of ±2.36 m, whereas the 1 m LiDAR DEM had a declustered mean of –0.11 m and standard deviation of ±0.75 m. Both have the same orders of magnitude as GPS-based measurements of conventional and LiDAR DEM errors obtained by other researchers. The 10 m error data were modeled using a two-component variogram with ranges of 20 and 1250 m, whereas the 1 m LiDAR error data were modeled using a single component variogram with a range of 125 m.

Sequential Gaussian simulation with normal score back transformation was used to model the 10 m DEM elevation error distribution. Twenty five simulated and equally probable elevation error maps were used to produce DEMs by subtracting each of the error maps from the original DEM, and the simulated DEMs were used to create slope angle maps, static factor of safety maps, Newmark critical acceleration maps, and Newmark displacement (D_N) maps for a hypothetical earthquake with an Arias intensity of I_A = 4 m/s. Slope angle standard deviations ranged from 0° to ±11°, with most values in the range of ±3° to ±5°. The observed elevation errors gave rise to considerable uncertainty in all of the derivative maps, with the standard deviations of calculated D_N values ranging from 0 to ±10 cm. The impact on landslide hazard zonation was examined by creating two maps. One classified any raster with a calculated mean $D_N \geq 10$ cm to be potentially unstable. The other used the results of the stochastic simulations to classify as unstable any raster having a ≥ 5% probability of $D_N \geq 10$ cm. The inclusion of uncertainty arising from the DEM elevation errors increased the area classified as unstable from 0.6% to 4.1% of the map area, suggesting the failure to account for DEM elevation errors may lead to serious underestimation of earthquake triggered landslide hazards.

Monte Carlo simulations based upon the observed LiDAR DEM elevation errors produced slope angle standard deviations of about ±3°, only slightly less than those obtained from the 10 m DEM even though the DEM grid spacing was reduced by an order of magnitude and the LiDAR elevation errors are noticeably less than the conventional 10 m DEM errors. This result is explained by a first-order, second-moment approximation for slope angle error, which shows a reciprocal scaling relationship between DEM grid spacing, DEM elevation error, and calculated slope angle error. Although LiDAR elevation errors may produce smaller slope angle errors than a conventional 10 m DEM, they too may have a significant effect on the reliability of earthquake triggered landslide hazard maps.

NON-TECHNICAL SUMMARY

External Award 04HQGR0035

INFLUENCE OF DIGITAL ELEVATION MODEL ERRORS ON THE RELIABILITY OF MAPS DEPICTING EARTHQUAKE-TRIGGERED LANDSLIDE HAZARDS

William C. Haneberg
Haneberg Geoscience, 10202 39th Avenue SW, Seattle WA 98146

(206) 935-0846
bill@haneberg.com

Global positioning system (GPS) surveying and computer simulations showed that errors in conventional USGS and laser (LiDAR) digital elevation models (DEM) covering part of Seattle introduce significant errors into the slope angle and stability calculations used to produce maps of earthquake-triggered landslide susceptibility. The results of this study suggest that unless the effects of elevation errors are taken into account, landslide susceptibility maps based on standard U.S. Geological Survey DEMs are of questionable reliability and may seriously underestimate landslide hazards. Although LiDAR DEM errors are smaller, they too have the potential to produce significant errors in landslide susceptibility maps.

OVERVIEW

REPORT FORMAT

The body of this report is presented in two parts, each of which was prepared for submission to a peer-reviewed scientific journal. Because each of the parts is a complete report in itself, there is some duplication between the two. Each part also has its own figure numbers, equation numbers, and reference list.

Part I describes the use of centimeter accurate global positioning system (GPS) surveying to measure elevation errors in a conventional 10 m digital elevation model (DEM) covering part of Seattle, Washington, and analyze the effects of those errors on grid-based seismic slope stability calculations of the type used by the U.S. Geological Survey and others to model the potential for earthquake triggered landsliding. It has been submitted to *Environmental & Engineering Geosciences*.

Part II describes a similar analysis of errors in a high-resolution (1 m) DEM produced using airborne laser scanning technology (also known as **Li**ght **D**etection and **R**anging, or LiDAR) covering essentially the same area as the 10 m DEM. At the time this report was written, Part II was being prepared for submission.

PROJECT PUBLICATIONS

Haneberg, W.C., 2004, Effects of digital elevation model errors on slope angle, static factor of safety, and Newmark acceleration uncertainty in GIS-style landslide hazard modeling: Geological Society of America *Abstracts with Programs*, Vol. 36, No. 5, p. 297.

Haneberg, W.C., submitted, Effects of digital elevation model errors on spatially distributed seismic slope stability calculations: an example from Seattle, Washington: *Environmental & Engineering Geoscience*.

Haneberg, W.C., in preparation, Elevation errors in a LiDAR DEM of an urban area: measurement and effects on geomorphic derivatives: for submission to *Geomorphology*.

In addition to the abstract and papers listed above, hour-long oral presentations describing the research were given at the University of Cincinnati, Western Washington University, and the Washington Section of the Association of Engineering Geologists.

DATA AVAILABILITY

The GPS data collected for this project are available as a tab-delimited text file or Microsoft Excel file from the PI (William C. Haneberg, Haneberg Geoscience, 10208 39th Avenue SW, Seattle WA 98146, bill@haneberg.com, 206 935-0846).

PART I— EFFECTS OF DIGITAL ELEVATION MODEL ERRORS ON SPATIALLY DISTRIBUTED SEISMIC SLOPE STABILITY CALCULATIONS: AN EXAMPLE FROM SEATTLE, WASHINGTON

INTRODUCTION

Spatially distributed applications of Newmark's (1965) sliding-block method using grids of slope angles calculated from digital elevation models (DEMs) are becoming the *de facto* standard for earthquake-triggered landslide assessment over broad areas (McCalpin; 1997; Mankelow and Murphy, 1998; Miles and Ho, 1999; Miles and Keefer, 2000; Jibson *et al.*, 2000; Refice and Capolongo, 2002). The accuracy and reliability of hazard maps produced using this approach depends in part on the accuracy of slope angles that are calculated from the DEMs and subsequently enter into the equations for both the static factor of safety against sliding and the Newmark critical acceleration. Bolstad and Stowe (1994), Fisher (1998), and Holmes *et al*. (2000), however, concluded that typical DEMs contain elevation errors large enough to have significant effects on slope angle calculations. Despite this knowledge, the possible effects of DEM elevation and slope angle errors are generally not considered even in cases where the variability of properties such as soil shear strength is formally incorporated into models of earthquake-triggered landslides (*e.g.*, van Westen and Terlien, 1996; Mankelow and Murphy, 1998; Refice and Capolongo, 2002). This is most likely a result of the difficulty and expense of adequately characterizing DEM elevation errors and assessing their effects on derivative calculations.

This paper describes the results of a field-based study of elevation errors in a U.S. Geological Survey 10 m DEM and their effects on a hypothetical Newmark slope stability model for an 18 km^2 portion of Seattle contained within the Duwamish Head 1:24,000 quadrangle (Figure 1). It builds upon previous research such as that by Holmes *et al.* (2000) and Fisher (1998) by a) measuring elevation errors in a network of closely spaced points in order to better understand the statistical behavior of DEM elevation errors at length scales as short as tens of meters, b) using a 10 m rather than 30 m (or coarser) DEM, and c) explicitly evaluating the effect of slope angle errors on Newmark seismic slope stability calculations. The work described in this paper does not, however, take into account the effects of slope angle errors that arise from the existence of small-scale, or sub-raster, topography that cannot be depicted on a discretely sampled DEM (Haneberg, in preparation).

Although LiDAR DEMs gridded at intervals less than 10 m are becoming increasingly common, and one is available for the area described in this paper (Haneberg, in preparation), their availability is far from universal. Conventional 10 m DEMs are far more common and, in many parts of the United States where DEM-based landslide hazard models might be useful, 30 m DEMs remain the standard (Ohlmacher and Davis, 2003; Haneberg, 2004a). Zhang and Montgomery (1994) concluded that, whereas 10 m DEMs represent substantial improvement over 30 and 90 m DEMs for hydrologic and

geomorphic modeling, 2 and 4 m gridded DEMs produced only marginally improved results. Therefore, 10 m DEMs typify the kind of off-the-shelf data that might be incorporated into an assessment of earthquake-triggered landslides in the United States.

DATA COLLECTION

Differential elevation and horizontal position data were collected using a pair of Ashtech ProMark 2 single-frequency (L1) GPS receivers. Both static and stop-and-go kinematic survey methods were used. The static data were recorded over intervals ranging from 18 minutes to 1 hour, depending on baseline length and positional dilution of precision (PDOP) at the time. About two-thirds of the static data were collected using one of the GPS receivers as a rover and the other as a base station occupying a known control point at a secure location within the study area, which produced baseline distances of 1 to 10 km. The control point was established using repeated observations of an hour or more with one of the GPS receivers and data from the nearby continuously operating reference stations (CORS) RPT1 and SEAW. The remaining one-third of the static points were established using one of the GPS receivers with the RPT1 and SEAW CORS as control points, producing baselines of 10 to 20 km. These static points were then used as initialization points for stop-and-go kinematic data collection using the second GPS receiver. All of the GPS data were processed using the manufacturer's proprietary Ashtech Solutions software, yielding 1660 data points consisting of NAD 83 UTM easting and northing along with an orthometric elevation calculated using the GEOID03 model.

The manufacturer's specifications for ProMark 2 survey accuracy are 0.005 m + 1 ppm baseline length (horizontal) and 0.010 m + 2 ppm baseline length (vertical) for static surveys (Thales Navigation, 2002). For stop-and-go kinematic surveys, the corresponding accuracies are 0.012 m + 2.5 ppm baseline length (horizontal) and 0.015 m + 2.5 ppm baseline length (vertical). Repeated observations of benchmarks and other known points suggest that both the accuracy and precision of the GPS data are in many cases on the order of millimeters and rarely more than a centimeter or two, making them accurate enough for comparison with DEM elevation values given to the nearest decimeter.

One disadvantage of working in an urban area is that it is difficult to generate a grid of randomly located GPS measurement points such as that used by Holmes *et al*, (2000), who conducted their study in a nature preserve. Data for this study were necessarily collected in publicly accessible areas such as streets, rights-of-ways, parks, and undeveloped parcels of land rather than on a truly random grid. Insofar as possible, GPS measurements points were also chosen so as to avoid multipath interference from overhead utility lines. Successful collection of the stop-and-go kinematic data required that both the rover and base units maintained a continuous lock on at least five satellites, which made it impossible to use that method beneath trees. Locations of the static and kinematic data points are shown in Figure 2.

RESULTS

Spatial Distribution of Errors

Elevation errors were calculated by transforming the DEM datum from NAD 27 to NAD 83, using an inverse squared distance algorithm to interpolate the 10 m DEM values onto a 1 m grid, reading the GPS elevation data into the same 1 m grid, and subtracting. The overall accuracy of the transformation was checked visually by overlaying a 1 m resolution orthophoto of the study area, a shaded relief map produced from the transformed DEM, and the control points.

The calculated DEM elevation errors ranged from –11.70 m to + 10.91 m, with a mean of –1.16 m and a standard deviation of ±1.87 m. This range is about half of that reported by Holmes *et al.* (2000) in their study of errors in a U.S. Geological Survey 30 m DEM and the standard deviation is similar to that reported by Fisher (1998) is his study of errors in a British Ordnance Survey 10 m DEM. The bias introduced by spatial clustering of GPS measurements was removed by cell declustering (Isaaks and Srivastava, 1989; Goovaerts, 1997), which produced a declustered mean of –0.92 m and declustered standard deviation of ±2.36 m at a cell size of 1600 m. Figure 3 shows histograms of the clustered and declustered data. There are weak correlations between the absolute value of the elevation error and both slope angle and elevation on the DEM (Figure 4). In both cases the regression lines are significant at the 0.001 level (ANOVA $p < 2 \times 10^{-16}$), but $r^2 = 0.12$ for error *vs*. slope angle and $r^2 = 0.07$ for error *vs*. elevation. Thus, the elevation errors appear to be largely, albeit not completely, independent of elevation and slope angle.

The spatial correlation structure of the elevation errors is shown by the empirical variogram in Figure 5. It was calculated using the Cressie and Hawkins (1980) robust estimator rather than the classical variogram estimator given in most geostatistics textbooks (*e.g.*, Isaaks and Srivastava, 1989; Goovearts, 1997) in order to account for the non-normality of the error data and the effects of outliers. Visual comparison showed that in this case the robust estimator produced a smoother variogram than did the classical estimator. Attempts to fit a simple single component model variogram using least-squares methods all yielded a physically unrealistic nugget of approximately 1 m. The empirical semivariance at a distance approaching zero should be equal to the instrumental accuracy, which is much less than 1 m, so a two-component variogram with no nugget was fitted by eye to the points separated by distances of 3000 m or less. The resulting model variogram, which is plotted along with the empirical variogram in Figure 5, is

$$\gamma(h) = 3.2\left\{1-\left[\frac{1.0}{3.2}\exp\left(-\frac{h}{20}\right)+\frac{2.2}{3.2}\exp\left(-\frac{h}{1250}\right)\right]\right\} \quad (1)$$

in which $\gamma(h)$ is the semivariance (m^2) and h is the lag, or distance between points (m). In order for the variogram to vanish at zero lag and simultaneously honor the empirical data at lags of tens to hundreds of meters, it was necessary to include a small-scale local

component (in this case with a range of 20 m) as well as a large-scale component with a range of 1250 m to reflect the overall trend of the empirical variogram. Fisher (1998) and Holmes *et al*. (2000) also found it necessary to use multi-component model variograms to adequately represent empirical DEM elevation error variograms.

Conditional Simulation of Errors

The spatial distribution of elevation errors was modeled using sequential Gaussian simulation (*e.g.*, Goovaerts, 1997; Holmes *et al*, 2000) based on the declustered mean and the model variogram given in equation (1). The method is conditional because it honors the location and value of known elevation errors and simulates normally distributed, or Gaussian, error values elsewhere. A normal score back-transformation was then applied to each set of simulation results, known as a realization, to produce output with the same statistical distribution as the measured errors. On the basis of the weak correlations described above, elevation error was assumed to be independent of elevation and slope angle. To obtain the results presented in this paper, each new simulated elevation error value was calculated using the nearest 20 known or previously simulated values. The gstat package for the open-source statistics software R (Pebesma and Wesseling, 1998; Pebesma, 2004) was used to obtain the error simulation results described in this paper.

A total of 25 elevation error realizations were calculated on a 1063 by 343 grid of points, of which 182,787 were on dry land, corresponding to the 10 m DEM grid in the study area. Five of the elevation error realizations are shown in Figure 6. All of the realizations show patterns of elevation error that are similar on a gross scale but differ in detail from map to map. The large-scale similarities reflect the spatial distribution of measured errors, which persist from simulation to simulation, whereas the small-scale differences reflect the randomness added by Gaussian simulation of values between the points at which elevation error was measured. Each error realization was subtracted from the DEM, which is assumed to consist of the true elevation at that point plus an unknown amount of error, to produce 25 different but equally probable realizations of the topography in the study area. Because the topographic realizations take into account measured elevation errors, each is in theory a more accurate representation of the real topography than the original DEM.

Figure 7 shows shaded relief images of the original 10 m DEM, the 10 m DEM with one elevation error subtracted, the average of 25 topographic realizations (DEM minus simulated errors), and, for comparison, a LiDAR DEM gridded at 3 m intervals. The most apparent effect of subtracting a single error realization from the DEM is an increase in noise, which obscures some geomorphic details visible in the original DEM. When a large number of error realizations are subtracted from the DEM and the results averaged, however, much of the random component of the noise disappears and the averaged DEM accentuates topographic subtleties that can be difficult to detect in the original DEM.

Effects on Derivative Maps

The topographic realizations were subsequently used to create 25 slope angle maps, 25 static factor of safety maps, 25 Newmark critical acceleration maps, and 25 slope displacement maps, from which sample mean and sample standard deviation maps were calculated for each map type. Four slopes were calculated for each DEM grid point using the eight surrounding elevations, and the maximum value was retained to represent the slope angle at each point. The static factor of safety against sliding was calculated for grid each point using the simplified infinite slope approximation

$$FS = \frac{c_T + \gamma_M T \cos^2 \beta \tan \phi}{\gamma_M T \sin \beta \cos \beta} \tag{2}$$

in which c_T is the total cohesion consisting of both soil cohesion and root strength (Pa), γ_M is the moist soil unit weight (N/m^3), ϕ is the angle of internal friction, T is the soil thickness (m), and β is the slope angle (degrees). In order to evaluate the effects of elevation and slope angle errors, all of the variables except slope angle were held constant across the study area and the effects of pore water pressure were not considered. The following values were chosen based upon a tabulation in McCalpin (1997) and a requirement of static stability throughout the study area: c_T = 10 kPa, γ_M = 19 kN/m^3, T = 2 m, and ϕ = 35°. Allowing the values to fluctuate randomly or vary according to location would have complicated the results and masked the effects of elevation errors, which enter into only the calculation of slope angle and Newmark accleration (and, indirectly, displacement). Haneberg (2000, 2004 a,b) discusses the additional uncertainty that is added by allowing the geotechnical parameters to behave as random variables.

Once slope angle and factor of safety maps were calculated for each of the 25 topographic realizations, 25 Newmark critical acceleration realizations were created using (Newmark, 1965)

$$a_N = (FS - 1) g \sin \beta \tag{3}$$

in which g is gravitational acceleration. The Newmark critical acceleration is threshold above which small increments of slope movement occur during an earthquake, and the displacement of the slope is estimated rigorously by twice integrating over time the portions of an accelerogram that lie above the threshold (Newmark, 1965; Jibson, 1993) or approximately by using empirical relationships incorporating variables such as a_N and Arias intensity (*e.g.*, Jibson *et al.*, 2000). The approximation used in this paper, obtained by fitting a curve to data from the 1994 Northridge, California earthquake, is (Jibson *et al.*, 2000)

$$\log D_N = 1.521 \log I_A - 1.993 \log a_N - 1.546 \tag{4}$$

in which D_N is the displacement (cm) of an unstable slope as the result of seismic shaking, I_A is the observed or predicted Arias intensity (m/s), and a_N is the Newmark critical acceleration with units of *g*. Additional uncertainties introduced by the use of equation (4), which had a strong but not perfect goodness-of-fit of $r^2 = 0.83$, were not considered. The results shown in this paper were calculated by assuming that $I_A = 4$ m/s uniformly across the study area. McCalpin (1997) assumed that landslides would occur in locations where $D_N \geq 5$ cm for sands and $D_N \geq 20$ cm for clays in Seattle. Jibson *et al.* (2000) found that 57% of the landslides in the 1994 Northridge, California earthquake occurred at locations with calculated $D_N \leq 5$ cm and 90% occurred at locations with $D_N \leq$ 10 cm.

Figure 8 shows the mean and standard deviation maps for slope angle, static factor of safety, Newmark critical acceleration, and displacement. The standard deviations of the calculated slope angles range from nearly zero to ±11°, with values most commonly in the range of ±3° to ±4°. Almost all of the values are ±6° or less. As shown in Figure 9, the slope angle standard deviations show a wide range of variability when plotted against the mean slope angle. The minimum standard deviations fall consistently within the range of ±1° to ±2°, but the maximum calculated slope angle standard deviation values decreased nearly linearly as a function of the mean slope angle. The slope angle errors propagate into static factor of safety and Newmark acceleration errors, the former as high as ±2.2 (with most values less than ±0.75) and the latter as high as ±0.52 *g* (with most values less than ±0.05 *g*). The final product of the Newmark analysis, the estimated displacement, ranges over $0.1 \geq D_N > 25$ cm, with most values calculated to be $D_N \leq 2$ cm or so. Most of the displacement standard deviations are ±5 cm or less, although some exceed 10 cm, with the values generally proportional the mean slope angle at each grid point. Previous work has shown that factors of safety at a point tend to better approximated by lognormal distributions than normal distributions, whereas Newmark critical acceleration values calculated using the factors of safety tend to be better approximated by symmetric normal distributions (Haneberg 2004 a,b). In order to determine whether the D_N values are better represented by a symmetric normal distribution or a positively skewed lognormal distribution, skewness values were calculated for each of the grid points. As shown in Figure 10, the distributions of results at the overwhelming majority of grid points are positively skewed. Skewness was negative at only 3596 of the 182,787 grid points, or less than 2% of the study area. Therefore, it is assumed that the D_N values at most grid points follow lognormal, or at least some kind of positively skewed, distributions.

Hazard Zonation Under Uncertainty

The incorporation of probabilistic results into hazard zonation schemes is complicated by the fact that the results are probability distributions (in this paper characterized by means and standard deviations) rather than single deterministic values that can be easily compared with a threshold. Consider the comparison of calculated probabilistic displacement values with a displacement threshold to determine whether or not a particular grid point should be classified as being susceptible to earthquake-triggered landsliding. For a lognormally distributed variable *x* with arithmetic mean $\bar{x}$

and standard deviation *s*, the value of *x* for which the probability of being exceeded equals *p* is (Appendix)

$$x = \exp\left\{\frac{1}{2}\left[2\log\bar{x} + 2\sqrt{2}\ \operatorname{erf}^{-1}(1-2p)\sqrt{\log\left(1+\frac{s^2}{\bar{x}^2}\right)} - \log\left(1+\frac{s^2}{\bar{x}^2}\right)\right]\right\} \tag{5}$$

in which erf^{-1} is the inverse error function. The probability that D_N is actually greater than its calculated mean, $\overline{D}_N$, at a grid point is found by setting (5) equal to the mean and solving for *p* to yield

$$p = \tfrac{1}{2}\left\{1 - \operatorname{erf}\left[\frac{\sqrt{\log\left(1+(s/\bar{x})^2\right)}}{2\sqrt{2}}\right]\right\} \tag{6}$$

For a normal distribution, the probability that a random variable takes on a value greater than its mean is always *p* = 50%. For a lognormal distribution, however, $p \to 0$ asymptotically as $s/\bar{x} \to \infty$ and $p \to 50\%$ asymptotically as $s/\bar{x} \to 0$ (Figure 11). Therefore, the probability of misclassifying a potentially unstable grid point as stable can be as large as that given by equation (6) if the hazard is determined by comparing the average displacement for each grid point to a threshold.

Calculated $s/\bar{x}$ ratios in the study area range over $0.00007 \le s/\bar{x} \le 9.8$, with values < 1 on tending to occur on steep slopes and values > 1 tending to occur on gentle slopes. This corresponds to maximum probabilities of misclassification ranging from 14% to 50%, which is unacceptable for two reasons. First, the maximum possible misclassification probability of 50% calls into question the utility of the hazard assessment that in the limit may not perform any better than the flip of a coin. Second, if the displacements at each point are lognormally distributed, or nearly so, the probability of misclassification will depend on the mean and standard deviation of the calculated displacements at each grid point and vary from point to point across the study area. Therefore, it is difficult to gauge the reliability of the results across the study area. A more consistent approach is to use equation (5) to set the probability of misclassification at an acceptably low level, say 5%, for each grid point. Similar procedures can be followed if the results are more faithfully replicated by a different probability distribution.

Figure 12 compares maps of the predicted landslide hazard for the study area subjected to the same hypothetical I_A = 4 m/s earthquake used to produce Figure 8, with a threshold displacement of 10 cm used to delineate the areas susceptible to landsliding. The left map, which is based on a comparison of the calculated mean displacement with a 10 cm threshold, predicts that 0.6% of the study area is susceptible to earthquake-triggered landsliding. The right map, which is based on a comparison of displacements that allow for no more than a 5% probability of misclassification with the threshold, predicts that 4.1% of the study area is susceptible to landslides during the hypothetical

earthquake. Most of the area added when the maximum permissible misclassification probability was reduced to 5% is in slightly to moderately hilly terrain rather than along the steepest slopes because, as discussed previously, steep slopes are characterized by low slope angle uncertainty. Much of the added area, therefore, might not be predicted to be susceptible based on a traditional qualitative geologic evaluation even though it must be considered susceptible if one adopts the maximum possible misclassification criterion used in this paper.

DISCUSSION

The results described in this paper show that DEM elevation errors propagate through each successive generation of derivative maps, although the magnitudes of the uncertainties arising as a consequence of elevation error vary both within and among maps. In general, comparison of the derivative maps with the original DEM or shaded relief map shows that the uncertainty tends to decrease as the mean slope angle increases. Haneberg (2004 a) used an analytical approximation of the slope angle variance to show that the decrease occurs because the elevation difference enters into the denominator of the approximation. Thus, there is a rational basis for the observation that any particular size of elevation error will have a greater effect on the calculated angle of a gentle slope than a steep slope. The same general relationship holds for calculated displacements, which tend to have smaller standard deviations in areas of steep slopes than in areas of gentle slopes. It is also notable that, with very few exceptions and regardless of the slope angle, there is a minimum slope angle standard deviation of ±1° to ±2° in the study area.

Based on the results in this paper as well as those of Bolstad and Stowe (1994), Fisher (1998), Holmes *et al.* (2000), and Wechsler and Kroll (submitted), elevation error standard deviations of plus or minus several meters and slope angle standard deviations of plus or minus several degrees should not be surprising in other areas. In practical applications of any GIS based models in which slope angle enters into the calculations, standard deviations on the order of at least ±3° to ±4° should be assumed to exist unless fieldwork proves otherwise. It is likely that the same magnitudes of uncertainties propagate into slope aspect and curvature calculations, which are widely used measures of quantitative geomorphology, although they were not evaluated as part of this study because they do not enter into seismic slope stability calculations. Slope angle standard deviations of several degrees can, as shown by a sensitivity analysis in Haneberg (2000), have an effect on static slope stability calculations that is on par with that caused by pore water pressure variations and angle of internal friction uncertainty. The observed degree of slope angle uncertainty also calls into question the practice of calibrating landslide hazard models to match inventory maps or physical expectations (*e.g.*, no landslides predicted for dry and static conditions) by adjusting variables such shear strength parameters while ignoring slope angle uncertainties, because without a detailed site investigation it is impossible to know how much each of the variables contributes to the mismatch.

Another practical implication of this work is that estimates of slope-related quantities will tend to be least reliable in marginal areas adjacent to steep and commonly

landslide prone hillsides such as coastal bluffs along Puget Sound. Therefore, engineering geologic and geotechnical characterization efforts may yield the greatest benefits if they are directed towards the reduction of uncertainty in marginal areas rather than confirming that steep slopes are indeed the most likely to move during a strong earthquake. Identification of marginal areas that merit further investigation is likely to be one of the most important applications of GIS based slope stability models regardless of whether the triggering mechanism is an earthquake, heavy precipitation, or human activity.

Finally, the work described in this paper emphasizes the fact that the results of any hazard assessment— regardless of whether it is based on qualitative geologic maps or quantitative computer simulations— have the potential to be wrong. Therefore, it is imperative to clearly consider the likelihoods and consequences of being wrong, to continue developing methods that allow practitioners to explicitly incorporate those likelihoods into their analyses, and communicating the likelihoods to end users who are ultimately responsible for the acceptance of risks.

ACKNOWLEDGEMENTS

The LiDAR data used in Figure 7 were provided by the Puget Sound Regional LiDAR Consortium.

APPENDIX

The cumulative distribution function for a lognormally distributed random variable x is

$$CDF(x) = \frac{1}{2}\left\{1 + \text{erf}\left[\frac{-\mu + \log x}{\sigma\sqrt{2}}\right]\right\} \tag{A1}$$

where the logarithmic mean, μ, and standard deviation, σ, are related to the aritimetric mean, $\bar{x}$, and standard deviation, s, by

$$\mu = \log \bar{x} - \frac{\sigma^2}{2} \tag{A2}$$

and

$$\sigma = \sqrt{\log\left(\frac{s^2}{\bar{x}^2} + 1\right)} \tag{A3}$$

To find the value of x that has probability of p or less of occurring, let

$$CDF(x) = 1 - p \tag{A4}$$

Then, substitute equations (A1), (A2), and (A3) into equation (A4) and solve for x, which yields

$$x = \exp\left\{\frac{1}{2}\left[2\log\bar{x} + 2\sqrt{2}\ \operatorname{erf}^{-1}(1-2p)\sqrt{\log\left(1+\frac{s^2}{\bar{x}^2}\right) - \log\left(1+\frac{s^2}{\bar{x}^2}\right)}\right]\right\} \quad \text{(A5)}$$

REFERENCES

Bolstad, P.V. and Stowe, T., 1994, An evaluation of DEM accuracy: elevation, slope, and aspect: *Photogrammetric Engineering & Remote Sensing*, v. 60, p. 1327-1332.

Cressie, N. and Hawkins, D.M., 1980, Robust estimation of the variogram: *Mathematical Geology*, v. 12, p. 115-125.

Fisher, P., 1998, Improved modeling of elevation error with geostatistics: *GeoInformatica*, v. 2, p. 215-233.

Goovaerts, P., 1997, *Geostatistics for Natural Resources Evaluation*: Oxford University Press, 483 p.

Haneberg, W.C., 2000, Deterministic and probabilistic approaches to geologic hazard assessment: *Environmental & Engineering Geoscience*, v. 6, p. 209-226.

Haneberg, W.C., 2004 a, A rational probabilistic method for spatially distributed landslide hazard assessment: *Environmental & Engineering Geoscience*, v. 10, p. 27-43.

Haneberg, W.C., 2004 b, *Computational Geosciences with Mathematica*: Springer-Verlag, 382 p.

Haneberg, W.C., in preparation, Multi-scale resampling of LiDAR DEMs to estimate the influence of sub-raster topography on slope angle errors.

Holmes, K.W., Chadwick, O.A., and Kyriakidis, P.C., 2000, Error in a USGS 30-meter digital elevation model and its impact on terrain modeling: *Journal of Hydrology*, v. 233, p. 154-173.

Isaaks, E.H. and Srivastava, R.M., 1989, *Applied Geostatistics*: Oxford University Press, 561 p.

Jibson, R.W., 1993, Predicting earthquake-induced landslide displacements using Newmark's sliding block analysis: Transportation Research Record, Paper 1411, p. 9-17.

Jibson, R.W., Harp, E.L., and Michael, J.A., 2000, A method for producing digital probabilistic seismic landslide hazard maps: *Engineering Geology*, v. 58, p. 271-289.

Mankelow, J.M. and Murphy, W., 1998, Using GIS in the probabilistic assessment of earthquake triggered landslide hazards: *Journal of Earthquake Engineering*, v. 20, p. 593-623.

McCalpin, J.P., 1997, *An Improved Procedure for Mapping Earthquake-Induced Landslide Potential Using a Geographic Information System, With Applications to the Puget Sound Region*: Geo-Haz Consulting, NEHRP Final Technical Report, Contract 11434-95-G-2550, 53 p.

Miles, S.B. and Ho, C.L., 1999, Rigorous landslide hazard evaluation using Newmark's method and stochastic ground motion simulation: *Soil Dynamics and Earthquake Engineering*, v. 18, p. 305-323.

Miles, S.B. and Keefer, D.K., 2000, Evaluation of seismic slope-performance models using a regional case study: *Environmental & Engineering Geoscience*, v. 6, p. 25-39.

Newmark, N.M., 1965, Effects of earthquakes on dams and embankments: *Geotechnique*, v. 15, p. 139-160.

Ohlmacher, G.C. and Davis, J.C., 2003, Using multiple logistic regression and GIS technology to predict landslide hazard in northeast Kansas, USA: *Engineering Geology*, v. 69, p. 331-343.

Pebesma, E.J. and Wesseling, C.G., 1998, Gstat: A program for geostatistical modelling, prediction and simulation. *Computers & Geosciences*, v. 24, p. 17-31.

Pebesma, E.J., 2004. Multivariable geostatistics in S: The gstat package. *Computers & Geosciences*, v. 30, p. 683-691.

Refice, A. and Capolongo, D., 2002, Probabilistic modeling of uncertainties in earthquake induced landslide hazard assessment: *Computers & Geosciences*, v. 28, p. 735-749.

Thales Navigation, 2002, *ProMark 2 Survey System, User's Guide for Surveying*: Santa Clara, California, Thales Navigation, 132 p.

Van Westen, C.J. and Terlien, M.T.J., 1996, An approach towards deterministic landslide hazard analysis in GIS, a case study from Manizales (Colombia): *Earth Surface Processes and Landforms*, v. 21, p. 853-868.

Wechsler, S.P. and Kroll, C.N., submitted, Quantifying DEM uncertainty and its effects on topographic parameters: *Photogrammetric Engineering & Remote Sensing*.

Zhang, W. and Montgomery, D.R., 1994, Digital elevation model grid size, landscape representation, and hydrologic simulations: *Water Resources Research*, v. 30, p. 1019-1028.

FIGURE CAPTIONS

Figure 1. Index map showing the general location of the study area.

Figure 2. Composite orthophoto and shaded relief image with locations of the static and kinematic stop-and-go GPS data points. UTM Zone 10 N grid ticks are shown along the upper and right margins.

Figure 3. Histograms of clustered and declustered elevation error estimates.

Figure 4. Plots showing relationship between the absolute values of the elevation error estimates and slope angle (upper) and elevation (lower), both calculated from the U.S. Geological Survey 10 m DEM covering the study area.

Figure 5. Empirical (open circles) and model (solid line) variograms illustrating the correlation of elevation error estimates separated by lag h. The expression for the model variogram is given in equation (1).

Figure 6. Five of the twenty-five elevation error realizations generated using conditional Gaussian simulation followed by a normal score back-transform.

Figure 7. Comparison of shaded relief images prepared using the original U.S. Geological Survey 10 m DEM, one elevation realization consisting of the 10 m DEM with one of the elevation error realizations subtracted, the average of 25 elevation realizations, and a LiDAR DEM gridded at 3 m intervals.

Figure 8. Results of Monte Carlo simulations performed using the 25 elevation error realizations. The top row shows mean value maps and the bottom row shows standard deviation maps. *FS* is the static factor of safety against sliding, a_N is the Newmark critical acceleration, and D_N is the Newmark displacement calculated using the empirical relationship of Jibson *et al.* (2000). Displacement was calculated using an assumed Arias intensity of $I_A = 4$ m/s across the study area.

Figure 9. Plot of slope angle standard deviations vs. mean slope angle, calculated from the slope angle maps in Figure 8.

Figure 10. Histogram of skewness values calculated for D_N distributions at each of the 182,787 grid points (some small and large values omitted for clarity).

Figure 11. Plot showing the maximum possible probability of misclassifying a potentially unstable grid point as stable if the classification is based on a comparison of the mean D_N with a threshold value, assuming a lognormal

distribution with arithmetic mean $\bar{x}$ and arithmetic standard deviation *s*. The large plot shows results for the values of $s/\bar{x}$ calculated for the study area. The small inset plot shows how the the maximum possible probability approaches zero as $s/\bar{x}$ grows large.

Figure 12. Maps showing predicted landslides (black dots) if the mean displacement exceeds the 10 cm threshold (left) and if the probability of misclassification is required to be less than 5% (right). The left map predicts that 1020 of the grid points will be unstable whereas the right map predicts that 7572 grid points will be unstable. Dots are shown larger than actual DEM grid size for visibility.

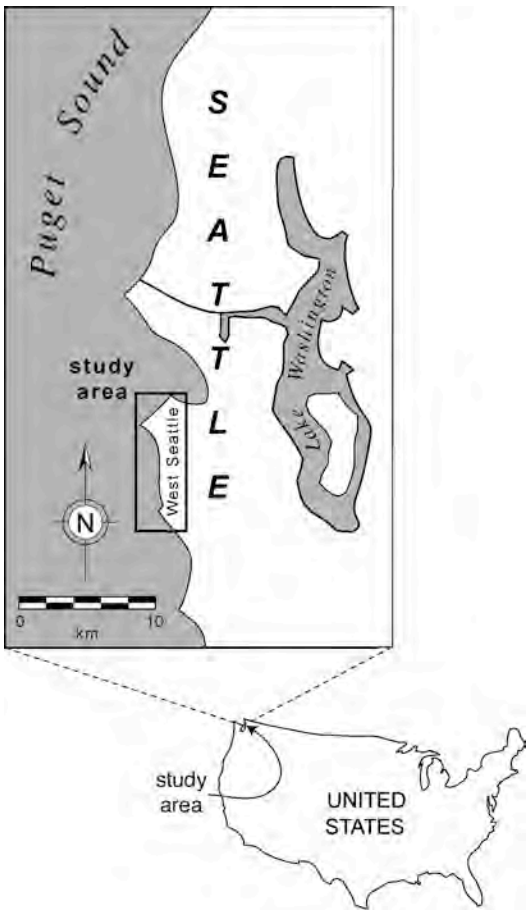
Puget Sound
SEATTLE
study area
West Seattle
Lake Washington
N
0
km
10
study area
UNITED STATES

Figure 1

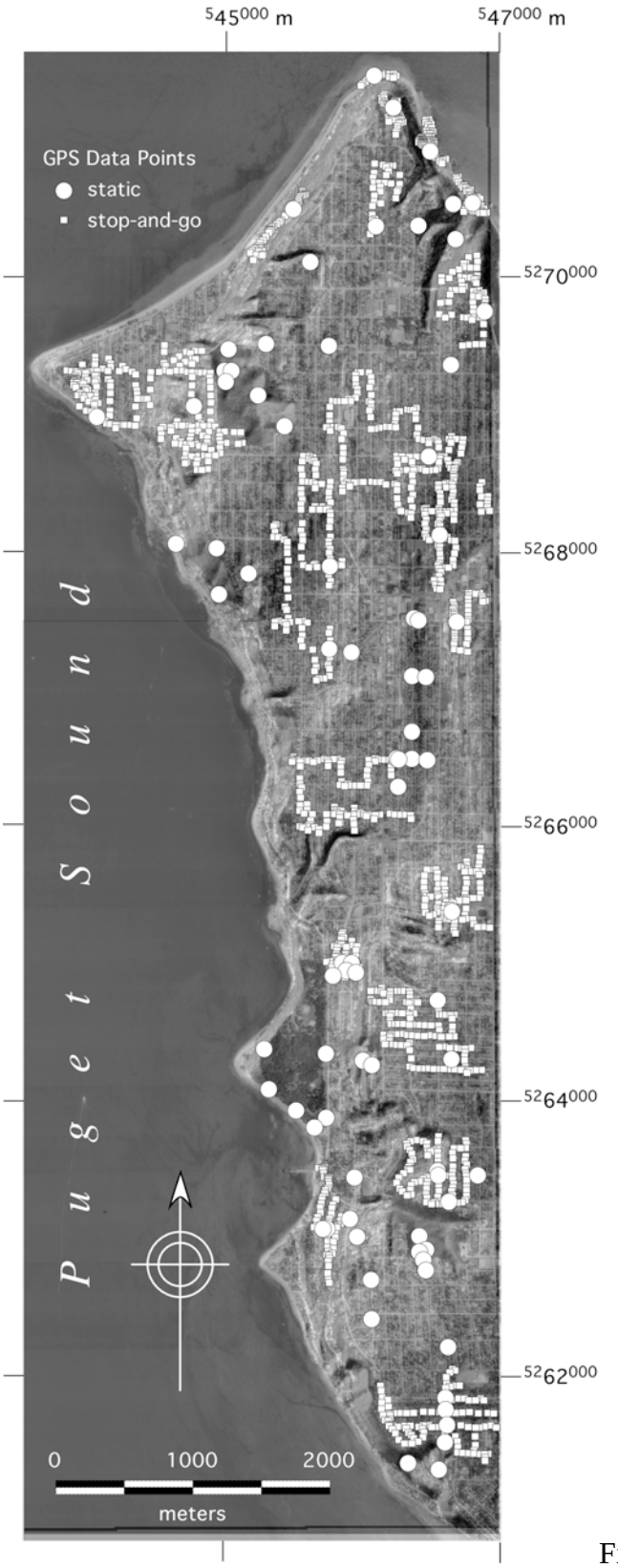
545000 m
547000 m
GPS Data Points
static
stop-and-go
5270000
5268000
5266000
5264000
5262000
Puget Sound
0
1000
2000
meters

Figure 2

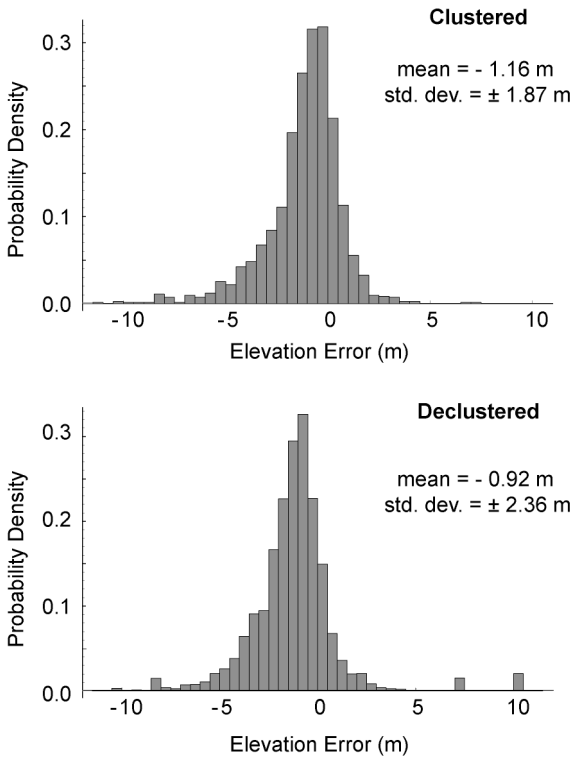
Clustered
mean = - 1.16 m
std. dev. = ± 1.87 m
Probability Density
0.3
0.2
0.1
0.0
-10
-5
0
5
10
Elevation Error (m)
Declustered
mean = - 0.92 m
std. dev. = ± 2.36 m
Probability Density
0.3
0.2
0.1
0.0
-10
-5
0
5
10
Elevation Error (m)

Figure 3

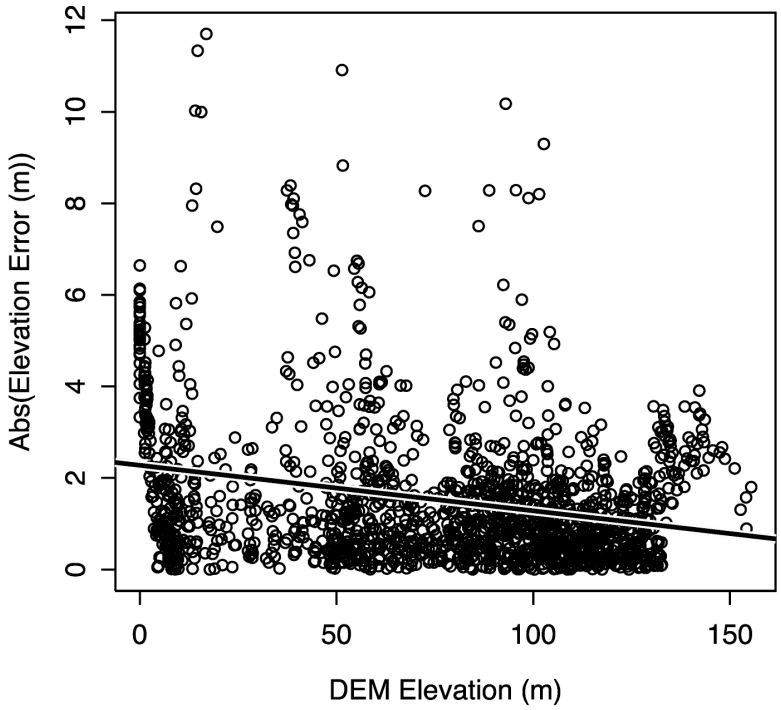
Abs(Elevation Error (m))
0
2
4
6
8
10
12
0
50
100
150
DEM Elevation (m)

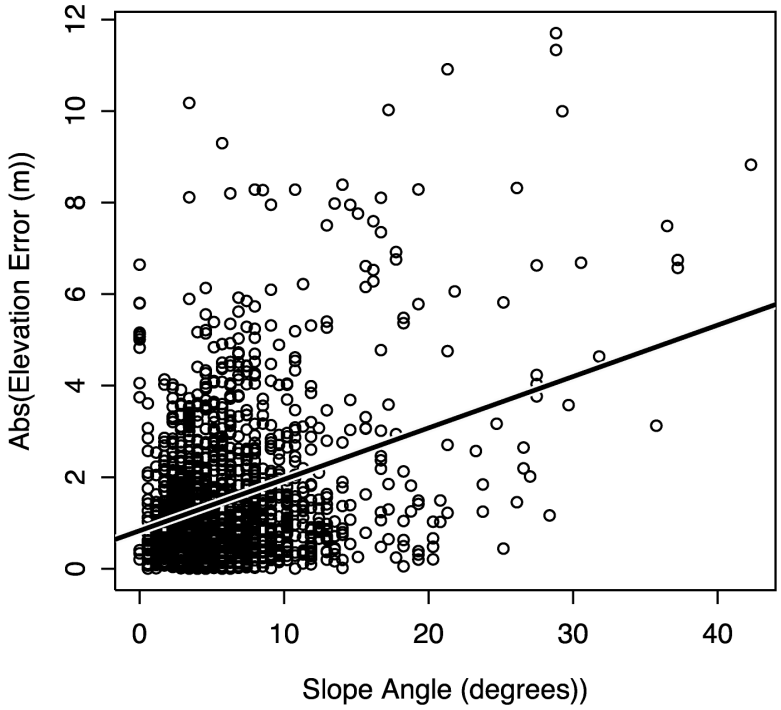
Abs(Elevation Error (m))
0
2
4
6
8
10
12
0
10
20
30
40
Slope Angle (degrees))

Figure 4

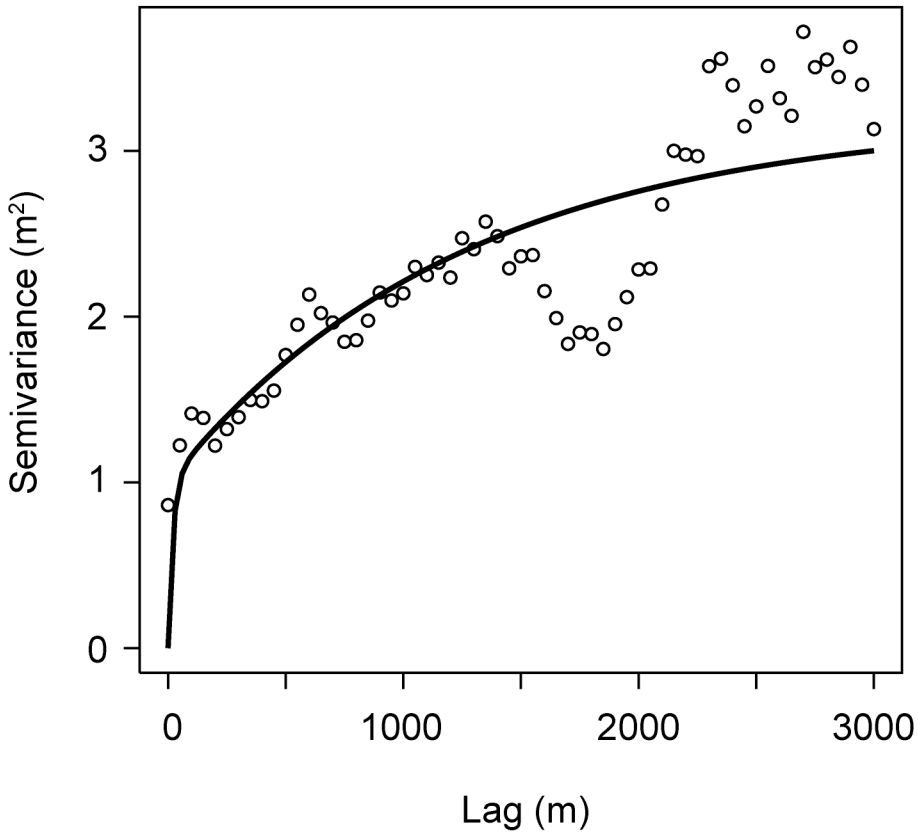

Figure 5

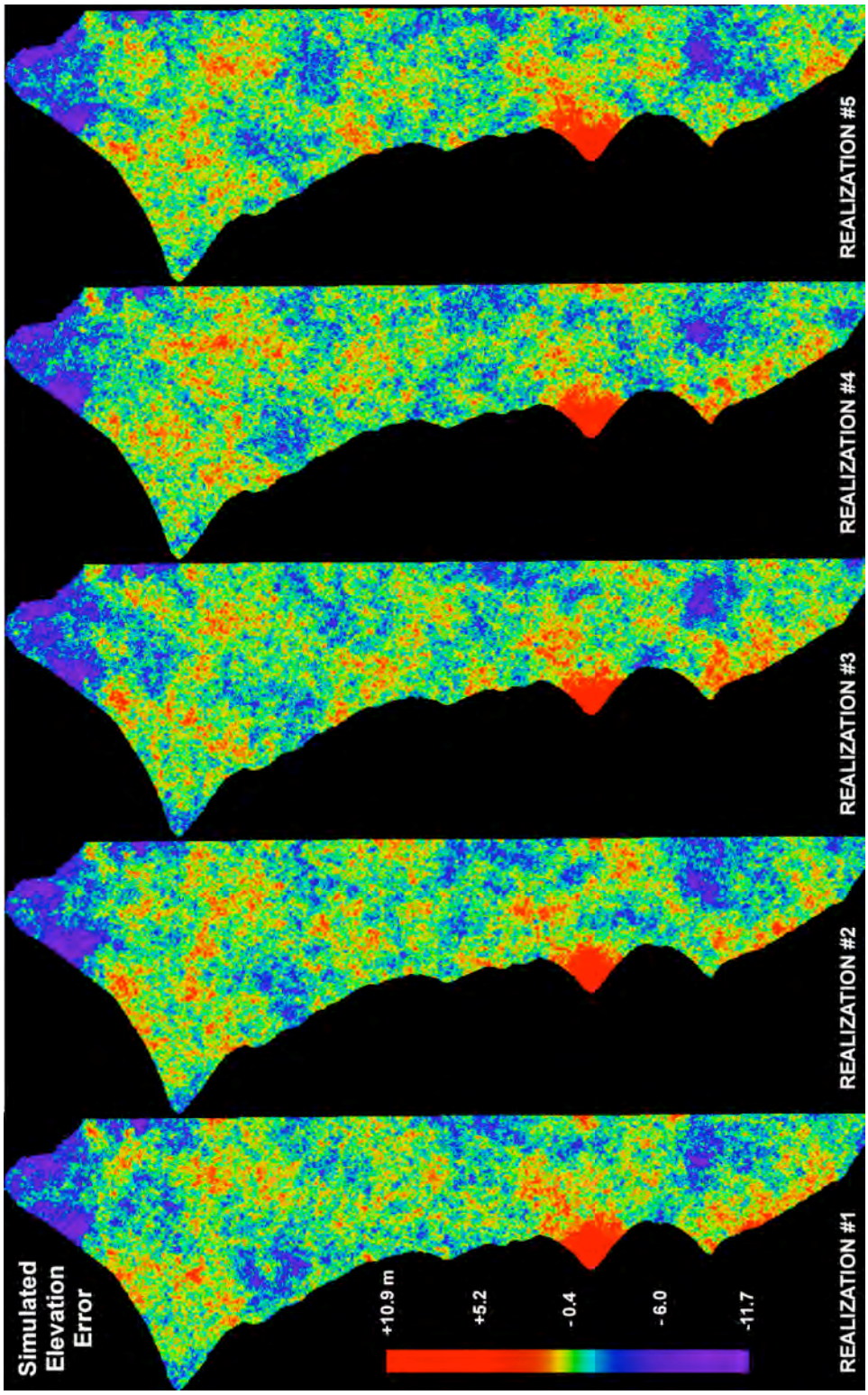
Simulated Elevation Error
+10.9 m
+5.2
- 0.4
- 6.0
-11.7
REALIZATION #1
REALIZATION #2
REALIZATION #3
REALIZATION #4
REALIZATION #5

Figure 6

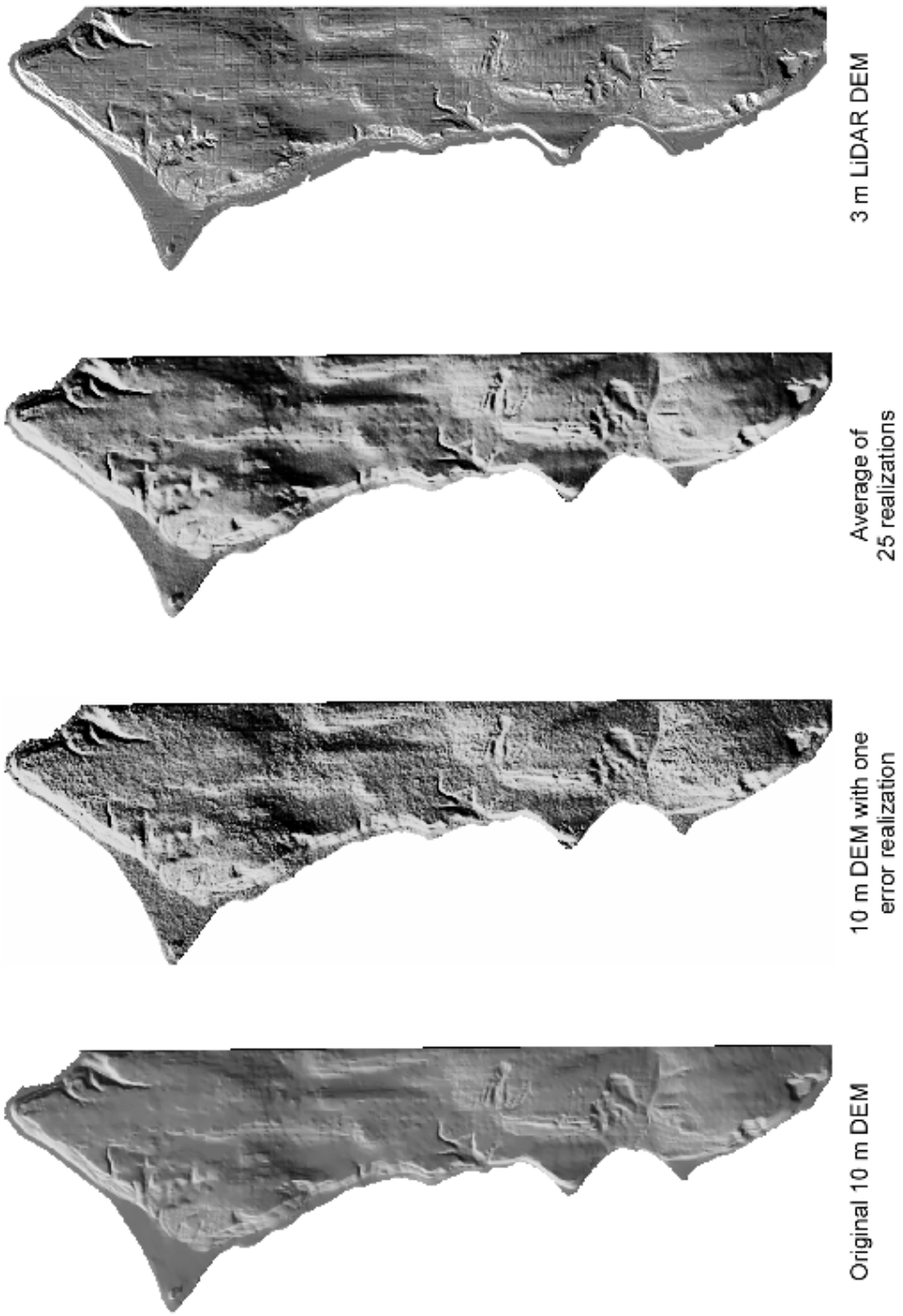
3 m LiDAR DEM
Average of
25 realizations
10 m DEM with one
error realization
Original 10 m DEM

Figure 7

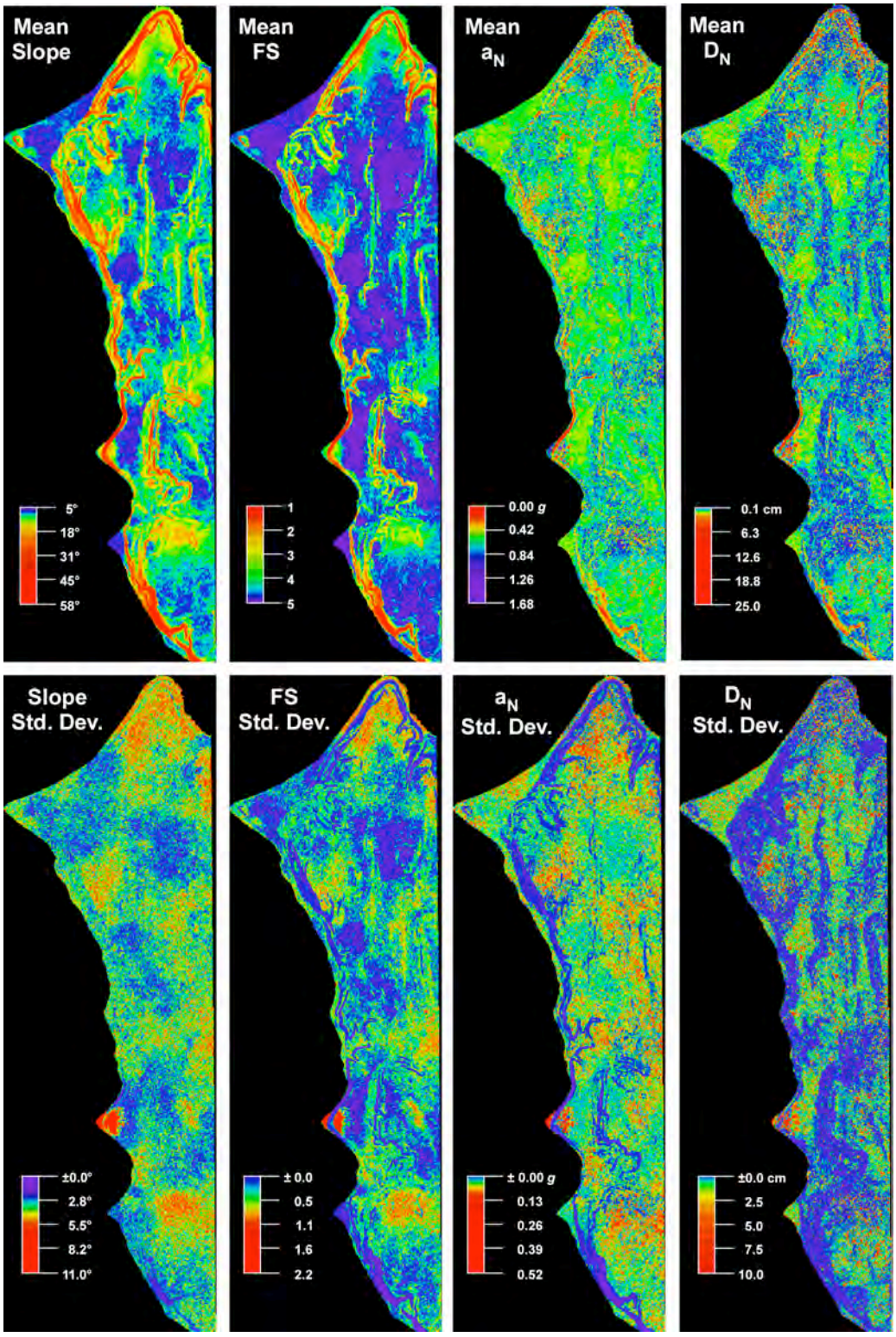
Mean Slope
5°
18°
31°
45°
58°
Mean FS
1
2
3
4
5
Mean a_N
0.00 g
0.42
0.84
1.26
1.68
Mean D_N
0.1 cm
6.3
12.6
18.8
25.0
Slope Std. Dev.
±0.0°
2.8°
5.5°
8.2°
11.0°
FS Std. Dev.
± 0.0
0.5
1.1
1.6
2.2
a_N Std. Dev.
± 0.00 g
0.13
0.26
0.39
0.52
D_N Std. Dev.
±0.0 cm
2.5
5.0
7.5
10.0

Figure 8

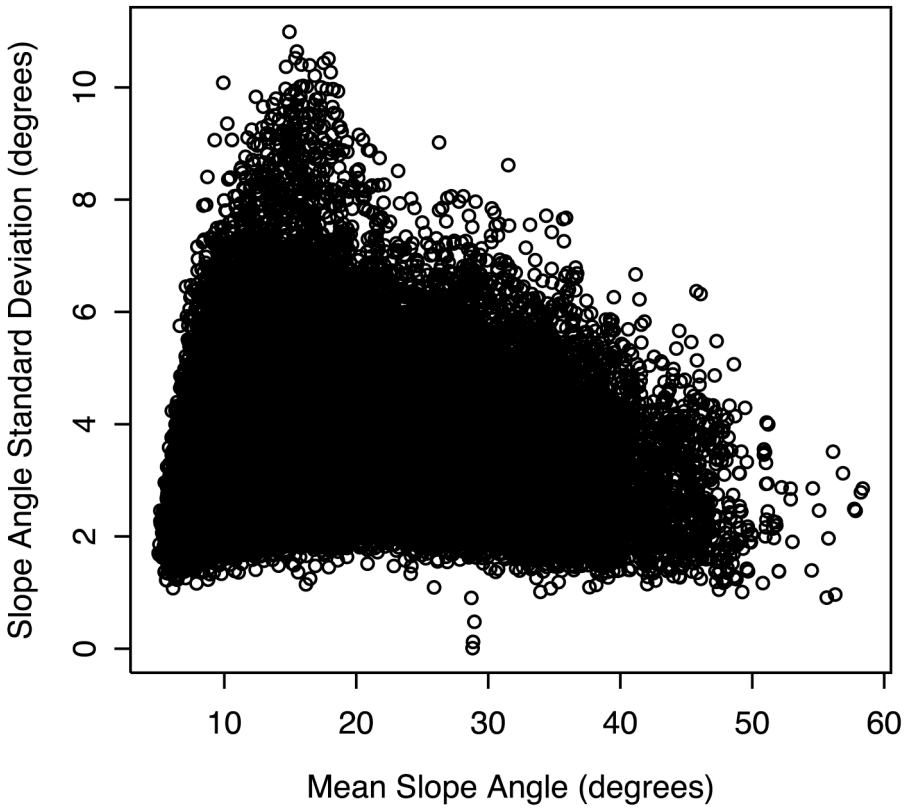
Slope Angle Standard Deviation (degrees)
0
2
4
6
8
10
10
20
30
40
50
60
Mean Slope Angle (degrees)

Figure 9

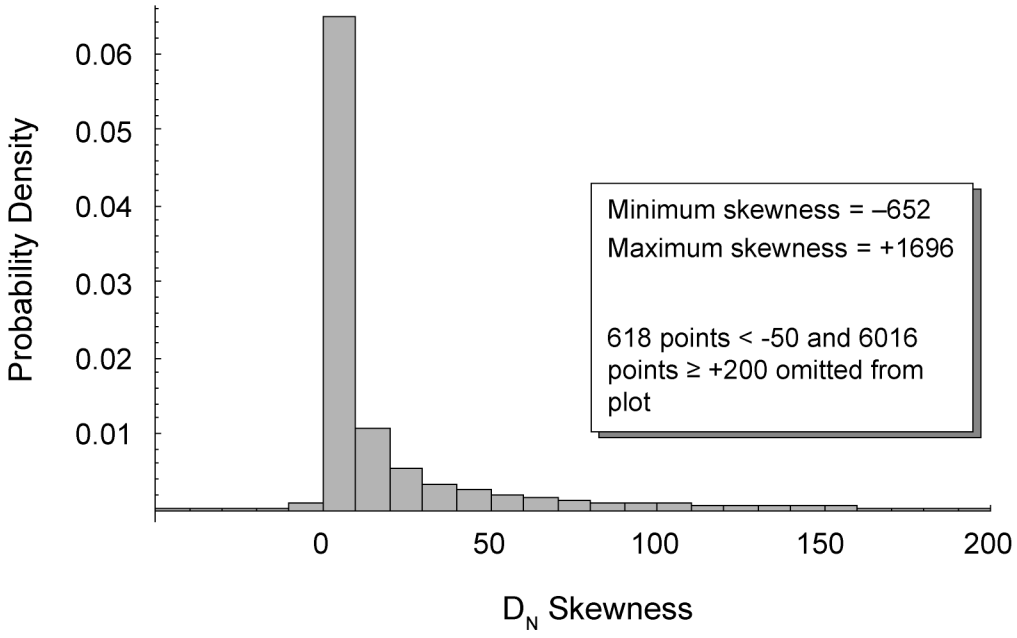
Probability Density
0.06
0.05
0.04
0.03
0.02
0.01
0
50
100
150
200
D_N Skewness
Minimum skewness = –652
Maximum skewness = +1696
618 points < -50 and 6016 points ≥ +200 omitted from plot

Figure 10

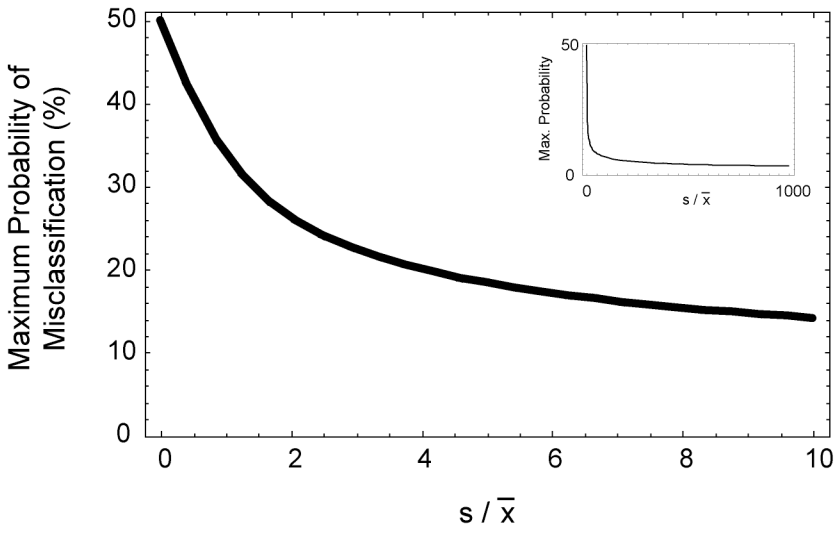
Maximum Probability of Misclassification (%)
50
40
30
20
10
0
0
2
4
6
8
10
s / x̄
Max. Probability
50
0
0
1000
s / x̄

Figure 11

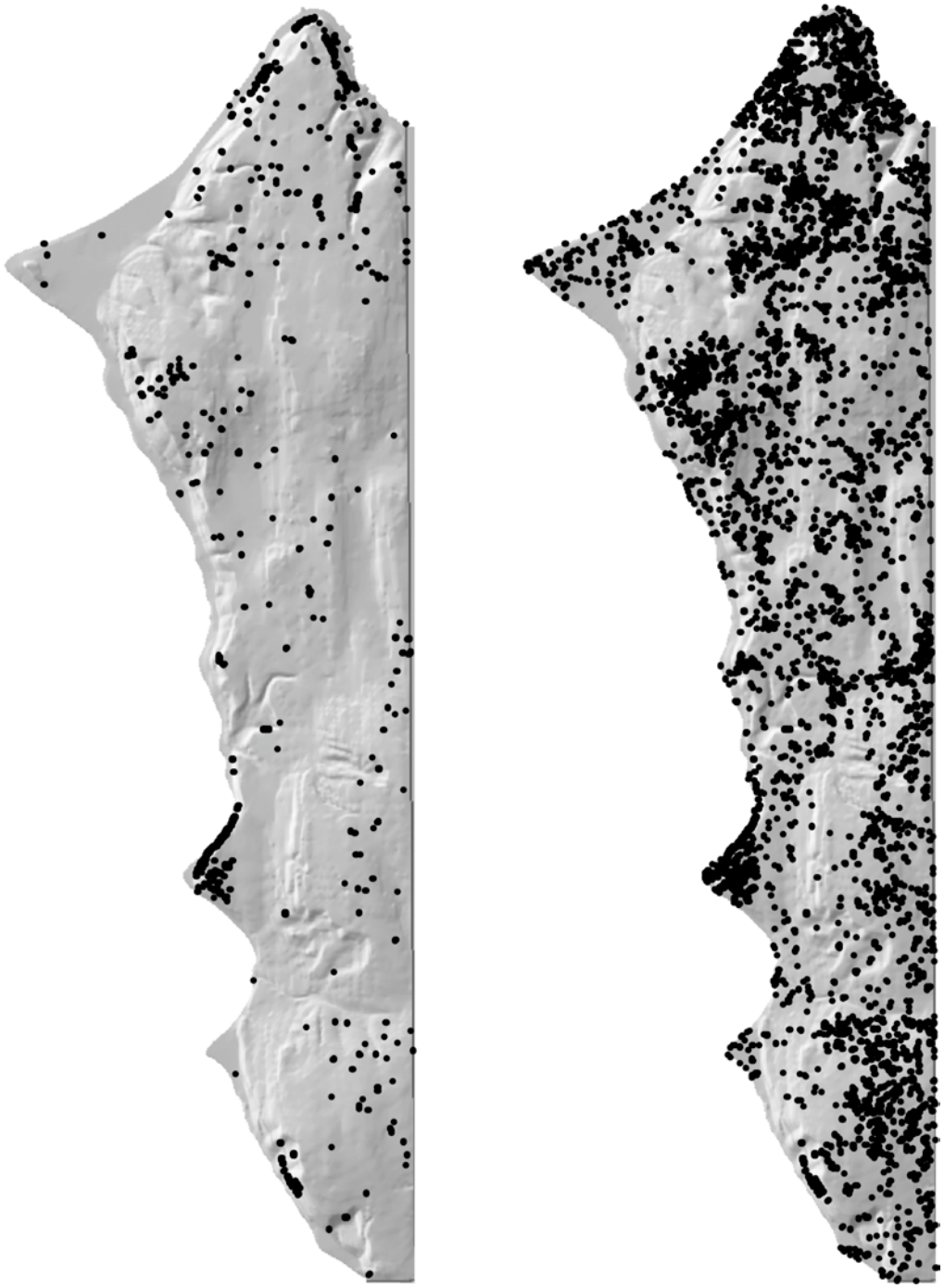

Figure 12

PART II— ELEVATION ERRORS IN A LIDAR DEM OF AN URBAN AREA: MEASUREMENT AND EFFECTS ON GEOMORPHIC DERIVATIVES

INTRODUCTION

One of the important geomorphological uses of digital elevation models (DEMs) is the generation of quantitative derivative maps based on the differences of adjacent elevation values, for example slope angle, slope aspect, slope curvature, topographic roughness, and residual topography maps. Derivative maps can be used for qualitative mapping of geomorphic units based on attributes such as local topographic roughness (Haneberg *et al.*, 2005; McKean and Roering, 2005), as input for rational and empirical evaluation of landslide, debris flow, and rock-fall hazards (Haneberg, in review, 2004; Baum, 2002; Guzetti *et al*., 2002; Holmes *et al.*, 2000; Sidle and Wu, 1999; Pack *et al.*, 1998; Shaw and Vaugeois, 1999; Montgomery and Dietrich, 1994; Ward *et al.*, 1981), and as input for runoff and erosion models (Cochrane *et al,* 2003; Tarboton, 1997; Quinn *et al.*, 1991).

Authors such as Haneberg (in review), Holmes *et al*. (2000), and Fisher (1998) have shown that the effects of elevation errors on slope angles and other derivative values calculated from conventional 10 m and 30 m DEMs can impart significant uncertainty into results. A few others, notably McKean and Roering (in review), Hodgson and Bresnahan (2004), and Adams and Chandler (2002) have evaluated LiDAR elevation errors using root-mean-square (RMS) statistics, but the geostatistical variability of high resolution LiDAR DEM elevation errors and their effects on geomorphic derivatives has not yet been examined. The work described in this paper 1) used more than 1700 centimeter accurate GPS measurements to estimate errors in a 1 m horizontal resolution LiDAR DEM covering a portion of Seattle, Washington, 2) used both kriging and stochastic simulation to visualize the spatial distribution of elevation errors across the study area, and 3) evaluated the effects of elevation errors on geomorphic derivative properties by using Monte Carlo simulations of the well-known Zevenbergen and Thorne (1987) equations for slope angle and slope aspect. The study area is essentially the same as that used by Haneberg (in review) for an evaluation of conventional 10 m DEM errors (and, in fact, uses a superset of the GPS measurements from that study), which also allows the two sets of results to be compared.

DATA COLLECTION

Study Area

The study area for this project is an 18 km^2 portion of Seattle, Washington known as West Seattle (Figure 1) and covered by the U.S. Geological Survey Seattle SW (formerly Duwamish Head) 7.5’ quadrangle. Relief in the area is about 155 meters, most of which occurs along coastal bluffs and a few deeply incised valleys. The study area consists of glacially striated uplands underlain primarily by till and outwash of the

Pleistocene Vashon glacial stage (Troost *et al.*, in review), in some places modified by landslides. Older glacial deposits and some bedrock are exposed locally, generally near the bottom of coastal bluffs. Land use is primarily urban residential, with some clusters of low-rise commercial buildings, schools, and parks (both open and heavily forested).

Global Positioning System Measurements

A total of 1723 differential elevation and horizontal position data were collected using two Ashtech ProMark 2 single-frequency (L1) GPS receivers. The manufacturer's specifications for ProMark 2 survey accuracy are 0.005 m + 1 ppm baseline length (horizontal) and 0.010 m + 2 ppm baseline length (vertical) for static surveys (Thales Navigation, 2002). For stop-and-go kinematic surveys, the accuracies are 0.012 m + 2.5 ppm baseline length (horizontal) and 0.015 m + 2.5 ppm baseline length (vertical). Repeated observations of benchmarks and other known points suggest that both the accuracy and precision of the GPS data are in many cases on the order of millimeters and rarely more than a centimeter or two. The general accuracy of survey points was also checked by overlaying them on a geo-referenced orthophoto with 0.5 m resolution after each day of data collection.

Both static and stop-and-go kinematic survey methods were used. The static data were recorded over intervals ranging from 18 minutes to 1 hour, depending on baseline length and positional dilution of precision (PDOP) at the time. About two-thirds of the static data were collected using one of the GPS receivers as a rover and the other as a base station occupying a known control point established at a secure location within the study area, which produced baseline distances of 1 to 10 km. The control point was established using repeated observations of an hour or more with one of the GPS receivers and data from the nearby continuously operating reference stations (CORS) RPT1 and SEAW. The remaining one-third of the static points were established using one of the GPS receivers with the RPT1 and SEAW CORS as control points, producing baselines of 10 to 20 km. These static points were then used as initialization points for stop-and-go kinematic data collection along a number of traverses using the second GPS receiver, which allowed for the rapid collection of many closely spaced data necessary to evaluate the effects of DEM errors on slope angle maps (Haneberg, in review). All of the GPS data were processed using the instrument manufacturer's Ashtech Solutions software, using NAD83 for the horizontal datum and NAVD88 for the vertical datum. Horizontal positions were calculated in Washington state plane coordinates and orthometric heights were calculated using the GEOID03 model incorporated into the Ashtech Solutions software.

One disadvantage of working in an urban area is that it is difficult to generate a network of randomly located GPS measurement points or to measure elevations at locations very close to lidar strike points as did Holmes *et al*. (2000), Hodgson and Bresnahan (2002), and McKean and Roering (in review), who conducted their studies in largely undeveloped areas. Data for this study were necessarily collected in publicly accessible areas such as streets, rights-of-ways, parks, and undeveloped parcels of land rather than on a random grid. As described below, statistical declustering was used to help eliminate the effects of non-random data locations when estimating global statistics.

Another potential problem with GPS surveys in many urban areas is interference with overhead utility lines. Insofar as possible, the GPS measurements points for this study were also chosen so as to avoid multipath interference from overhead utility lines. Successful collection of the stop-and-go kinematic data required that both the rover and base units maintained a continuous lock on at least five satellites, which also made it impossible to use that method beneath trees. Locations of the static and kinematic data points are shown in Figure 2.

Digital Elevation Model Creation

The DEM used for this project was created from *x,y,z* bare-earth points supplied by the Puget Sound LiDAR Consortium (PSLC). The LiDAR data were originally obtained by a private contractor using a multiple-return laser scanner mounted in a fixed-wing aircraft, with an on-the-ground laser spot of approximately 0.9 m, pulse spacing of 1.5 m, and 50% overlap between adjacent flight lines. This produced coverage with an average density of approximately 1 pulse/m^2 and a stated vertical accuracy of approximately 0.30 m (with the caveat that the accuracy is likely to be less in some areas).

The *x, y, z* points were supplied with units of U.S. survey feet in the Washington state plane coordinate system and NAD 83 datum (1991 HPGN adjustment). They were imported into a sparse 1 m (3.2808 feet) raster grid that was filled using inverse distance squared interpolation. Horizontal coordinates were converted from U.S. survey feet to meters by recalculating coordinates for the four corners of the DEM and changing the raster size units. Neither the datum nor the coordinate system was changed by this procedure. Heights were converted from feet to meters by simple multiplication. As received from PSLC, the LiDAR data included several clusters of elevation values for the waters of Puget Sound. Therefore, the final step of DEM creation was to remove elevations less than 2.5 m in order to eliminate most of the spurious values. This also had the effect of removing 4 of the 1723 GPS elevation measurements. The final DEM thus contained 19,871,336 elevation points for comparison against 1719 GPS measurements.

ELEVATION ERRORS

Method of Calculation

Elevation errors were calculated for each 1 m raster containing a GPS measurement by subtracting the DEM value for that raster from the GPS value, and the entire difference was attributed to DEM elevation error (*cf.* Hodgson and Bresnahan, 2004). This procedure lumps together true LiDAR vertical errors, true LiDAR horizontal errors, DEM interpolation errors, and GPS surveying errors. This study assumes that GPS surveying errors are on the order of a centimeter or two, or about the same order of magnitude as interpolation errors, based upon both the manufacturer's instrument specifications and field testing. Thus, the calculated elevation error values represent the total LiDAR DEM error, which is different than the LiDAR point error and potentially more relevant to geomorphic modeling projects based on LiDAR DEMs than point error

measurements. As described below, the errors calculated during this project were compared with geomorphic factors such as slope angle and topographic roughness but no attempt was made to subdivide errors on the basis of ground cover or land use.

Global Statistics

The calculated elevation errors ranged from –4.88 m to +3.32 m, with the majority falling in the range of ±0.5 m. Both clustered and unclustered summary statistics were calculated for the elevation errors in order to account for the non-random sampling pattern. The clustered error data had a mean of –0.03 m and a standard deviation of ±0.65 m, and cell declustering (Isaaks and Srivastava, 1989) produced an unclustered mean of –0.11 m and an unclustered standard deviation of ±0.75 m (Figure 3).

There are no strong relationships between the magnitude of elevation error and elevation, maximum slope angle, slope aspect, or topographic roughness (Figure 4). The maximum slope angle for each raster was defined as the largest of the four finite difference slope values calculated from the eight neighboring rasters. Topographic roughness was calculated using the method described by Haneberg *et al*. (in press), in which roughness is defined as the standard deviation of residual topography within a moving window of specified size (in this case 5 by 5 rasters). Residual topography, in turn, was defined as the difference between the 1 m DEM elevations and a topographic map smoothed with a 5 by 5 raster averaging window. Linear regression showed that there are statistically significant ($p \leq 0.05$) relationships between the absolute value of elevation error and elevation, slope angle, and topographic roughness but not slope aspect (Table 1). The goodness of fit was low to virtually nonexistent in all three cases for which a statistically significant relationship exists, however, and these relationships therefore have little explanatory power. Taken together, they account for only 30% of the variability of the elevation error.

Table 1. Linear regression results for the absolute value of elevation error as a function of four different independent variables.

	Intercept	**Slope**	r^2	p
Elevation	0.33	0.0010	0.0057	0.001
Slope Angle	0.10	0.024	0.19	$< 2.2 \times 10^{-16}$
Aspect Angle	0.46	-0.00021	0.0014	0.06
Roughness	0.18	3.00	0.11	$< 2.2 \times 10^{-16}$

Spatial Correlation Structure

North-south, east-west, and omnidirectional empirical variograms were calculated using the Cressie and Hawkins (1980) robust method to account for the non-normality of the error data and the effects of outliers. Each of the two directional variograms has an angular tolerance of ±22.5°. The elevation errors exhibit a well-developed north-south spatial correlation structure, parallel to the glacial fabric of the topography, with a variogram range of about 1500 m (Figure 5A). The east-west spatial correlation structure,

which is perpendicular to the glacial fabric, is weak to non-existent and the variogram quality decays at lags greater than several hundreds of meters (Figure 5B). The decay is most likely related to the small number of data points separated by large lags in the east-west direction, which is a consequence of the study area shape. The omnidirectional variogram (Figure 5C) shows a well-developed spatial correlation structure that was modeled using a least-squares best-fit exponential variogram with a range of 125 m and a sill of 0.21, or

$$\gamma(h) = 0.21\left[1 - \exp\left(-h/125\ \text{m}\right)\right] \quad (1)$$

in which γ is the semi-variance of the elevation errors and h is the lag, or separation distance, in meters. The model variogram sill corresponds to an elevation error standard deviation of ±0.65 m, which identical to that calculated from the clustered error data and slightly smaller than the value of ±0.75 calculated from the unclustered error data.

Estimation and Simulation

The distribution of elevation errors across the entire study area was approximated using two different methods: local kriging estimation and Monte Carlo simulation based upon sequential Gaussian simulation (Isaaks and Srivastava, 1989; Goovaerts, 1997). Both methods were based on the omnidirectional model variogram described by equation (1), and calculations were performed using the gstat package for the open-source statistics software R (Pebesma, 2004). Kriging estimates the elevation errors at specified points using a weighted linear combination of nearby measured error values (in this case the 100 nearest values) in a way that minimizes the estimated misfit between the kriged values and the unknown true values (*nb.*, the misfit is commonly referred to as the kriging error, but is renamed here because the variable being simulated is itself an error and it is confusing to refer to two different kinds of errors with similar names). Kriged estimates of the elevation error were calculated for each point on a regular 10 m grid covering the entire study area (computer memory limitations ruled out the use of 1 m grids for this portion of the project). Monte Carlo simulation generates a number of random simulations, or realizations, of the error distribution from which a mean and standard devation (or variance) can be calculated at each simulation point. In this study, as in Haneberg (in review) and Holmes *et al.* (2000), the random simulations were generated using sequential Gaussian simulation with normal score back transformation. Sequential Gaussian simulation honors the known error measurements and simulates the error at other points using a normal distribution (described by the global mean and variance) and a model variogram (in this case as described by equation (1)). Nearby known and previously simulated values are used to simulate new values on a regular grid. Normal score back-transformation is then used to map the normally distributed results back onto the observed error distribution. As with the local kriging estimates, the sequential Gaussian simulation results described in this paper are based on values calculated using the 100 nearest neighbors. An ensemble of 25 simulations was then used to calculate the mean and standard deviation of the simulated error at each point on a regular 10 m grid.

Results of both the local kriging and Monte Carlo simulations are shown together in Figure 6 so that they can be easily compared. Kriging produces a relatively smooth elevation error surface punctuated by many localized highs and lows (Figure 6A) and on which the uncertainty of the kriged values, as reflected by the kriging misfit standard deviation, increases sharply with distance to the nearest known point (Figure 6B). This is a direct consequence of the short variogram range of 125 m and the larger distances between clusters of elevation measurements. Four of the 25 random realizations are shown for comparison in Figure 6C-F, with the mean and standard deviation maps for all 25 simulations shown in Figure 6 G,H. Comparison of the kriged error map and the realizations shows that each of the four random simulations is essentially a very noisy version of the kriged distribution. Averaging the 25 simulations to calculate the simulated means produces a map that is less noisy than any one of the individual simulations but still more complicated than the kriged map. Like the kriging standard deviation, the simulated error standard deviation increases with distance from known points and the GPS survey traverses can be discerned as areas of smaller standard deviations.

EFFECTS ON GEOMORPHIC DERIVATIVES

The effect of DEM elevation errors on derivative calculations is tempered by the facts that the errors seem to be correlated over distances ranging from meters to kilometers (Haneberg, in review; Holmes *et al*., 2000; Fisher, 1998) and that derivatives are calculated from neighboring elevation values separated from each other by distances on the order of the DEM grid spacing, Δx, for example $2\Delta x$ in slope angle and aspect calculations (Zevenbergen and Thorne, 1987). The relevant measure of elevation error or uncertainty is therefore the variance or standard deviation of DEM elevation errors among grid points located $2\Delta x$ apart, not the global variance or standard deviation.

The semi-variance of a spatially correlated variable, in this case the elevation error $\varepsilon(x)$, is related to the expected or mean value and variance of the elevation errors at points separated by lag *h* (Isaaks and Srivastava, 1989; Goovaerts, 1997), or

$$\gamma(h) = \tfrac{1}{2}\mathrm{E}\left\{\left[\varepsilon(x) - \varepsilon(x+h)\right]^2\right\} = \tfrac{1}{2}\mathrm{Var}\left\{\varepsilon(x) - \varepsilon(x+h)\right\} \qquad (2)$$

in which $\gamma(h)$ is the semi-variance of the elevation errors, E is the expectation operator, Var is the variance operator, and *h* is the lag, or distance between pairs of elevation values. For slope angle and aspect calculations, $h = 2\Delta x$ and equation (2) can be rearranged to give the variance of elevation errors among points located $2\Delta x$ from each other, which is

$$\mathrm{Var}\left\{\varepsilon(x) - \varepsilon(x+2\Delta x)\right\} = 2\gamma(2\Delta x) \qquad (3)$$

For the model variogram given by equation (1), the elevation error variance appropriate for geomorphic derivative calculations on a 1 m grid (*h* = 2 m) is $6.7 \times 10^{-3}\mathrm{m}^2$. Its square

root, the elevation error standard deviation, is ±0.082 m. This is slightly more than one-tenth of the global variance.

The effect of DEM elevation errors on slope angle and slope aspect calculations was evaluated using a series of Monte Carlo simulations. In each of the simulations, elevation errors were randomly selected from a normal distribution with a zero mean and a standard deviation of ±0.082 m, consistent with the values measured in this study, and then added to a grid of elevation values defining a north-facing plane with a slope angle of 0°, 10°, or 20°. Slope angle and aspect were then calculated for each of the hypothetical slopes using the Zevenbergen and Thorne (1987) equations, and the process was repeated to produce an ensemble of 1000 slope angle and aspect calculations for each of the three slopes.

Results are shown as a series of histograms in Figure 7. Elevation errors of the same magnitude as those measured in this study produced slope angle standard deviations of ±2° to ±3° and simulated slope angles followed symmetric normal-like distributions. Monte Carlo mean slope angles for the 10° and 20° slopes were accurate to the nearest degree, but the calculated mean slope angle for 0° plane was 4° and simulation results followed a positively skewed lognormal-like distribution. The skewness and erroneous mean calculated for the 0° slope arise because elevation errors can either increase or decrease the steepness of an inclined plane, but can only increase the steepness of a perfectly horizontal plane. Slope aspect errors exhibited a different kind of behavior as the true slope angle increased from 0° to 20°. The calculated mean was consistently accurate to the nearest degree for all three hypothetical planar slopes. The calculated standard deviations follow a nearly uniform distribution with a standard deviation of ±103° for the 0° plane to ±9° for the 20° plane, but follow a symmetric normal-like distribution with a standard deviation of ±21° for the 10° slope and a very tightly grouped symmetric distribution with a standard deviation of ±9° for the 20° slope.

With the exception of the skewed 0° slope results, the simulated slope angle errors agree with slope angle errors predicted using the first-order, second-moment approximation developed by Haneberg (2004) for use with finite difference slope angle calculations typically used on DEMs (*e.g.*, Zevenbergen and Thorne, 1987). Rewritten in terms of the slope angle standard deviation, Haneberg's (2004) approximation is:

$$s_\beta = \frac{180}{\pi} \frac{\sqrt{8}\, s_\varepsilon \Delta x}{4\Delta x^2 + \left(z_{r,c+1} - z_{r,c-1}\right)^2 + \left(z_{r+1,c} - z_{r-1,c}\right)^2} \tag{4}$$

in which s_β is the standard deviation of the slope angle in degrees, s_ε is the standard deviation of the elevation errors for the four points used in the slope angle calculation, separated by Δx is the DEM grid spacing, z is elevation, and r and c are the DEM row and column indices. Equation (4) assumes that the elevation error standard deviation is the same for all four elevation values used in the calculation. The presence of elevation differences in the denominator of equation (5) implies that the elevation error should

decrease slightly as the slope angle increases. Figure 8 shows the relationship defined in equation (5) as a function of summed squared elevation differences

$$\Delta z^2 = \left(z_{r,c+1} - z_{r,c-1}\right)^2 + \left(z_{r+1,c} - z_{r-1,c}\right)^2$$

for slope angles calculated from a 1 m DEM grid with an elevation error standard deviation of ±0.082 m. Superimposed on the plot are the three Monte Carlo results from Figure 7 in addition to a fourth simulation for a 45° plane.

DISCUSSION

Centimeter-accurate GPS surveying has shown that elevation errors in a 1 m LiDAR DEM covering a portion of Seattle have an unclustered mean of –0.11 m, which slightly better than the stated accuracy of ±0.30 m supplied in the LiDAR metadata, and an unclustered standard deviation of ±0.75 m. This standard deviation is two to three times the root mean square errors reported by Hodgson and Bresnahan (2004), Adams and Chandler (2002), and McKean and Roering (in review), and slightly less than the ±0.84 m standard deviation reported by Norheim *et al.* (2002) in their assessment of lidar DEM errors in an area northeast of Seattle. By way of comparison, it is also considerably smaller than the standard deviation of ±2.36 m reported by Haneberg (in review) from his study of elevation errors in a conventional 10 m DEM covering the same area and the values reported by Fisher (1998) and Holmes *et al.* (2000) in their analyses of 10 m and 30 m DEMs from other areas.

The measured elevation errors are positively but weakly correlated with slope angle. topographic roughness, and, to a lesser degree, elevation. In all three cases r^2 values are low and the relationships have little explanatory power, accounting for no more than 30% of the elevation error variability. To a first approximation, therefore, the elevation errors measured in this study can be considered to be largely independent of elevation, slope angle, slope aspect, and topographic roughness.

Another significant difference between the LiDAR DEM elevation errors described in this paper and conventional DEM elevation errors described elsewhere is the spatial correlation structure. The errors described in this paper were modeled by a single component variogram with a range of 125 m, whereas the conventional DEMs analyzed by Haneberg (in review), Fisher (1998), and Holmes *et al.* (2000) required multi-component variograms with ranges on the order of a kilometer. The small variogram range means that, although the global mean and variance can be estimated using a relatively small number of randomly located measurements (perhaps something on the order of 10^2 points), elevation measurements must be closely and uniformly spaced if the spatial variability of elevation errors is a significant concern. The points must be closely spaced in order to obtain large numbers of pairs separated by distances less than 10^2 m, which is the order of magnitude of the variogram range obtained in this study. If elevation measurements are clustered, as they necessarily were in this study, then the reliability of error measurements across the study area will be variable. An ideal LiDAR

DEM elevation error network that is both dense and uniform would consist of measurement locations separated from each other by no more than a few tens of meters in order to adequately characterize the empirical error variogram at lags of 10^0 to 10^2 m. This would amount to many tens of thousands of elevation error measurements for a study covering an entire 7.5' topographic quadrangle.

Elevation errors of the magnitude described in this study can impart significant errors into slope angle and slope aspect calculations based on high resolution DEMs. This is particularly important if slope angle, aspect, flow direction, or other derivative maps are as used input for GIS-based models in a regulatory setting, because slope angle standard deviations of several degrees can have a significant effect on output. The magnitude of slope angle errors arising from elevation errors in the high-resolution LiDAR DEM used in this study are only slightly smaller than those calculated for conventional 10 m and 30 m DEMs by Haneberg (in review), Holmes *et al.* (2000), and Fisher (1998). Although a high resolution LiDAR DEM is capable of representing smaller scale topographic features than a more coarsely gridded conventional DEM, and thus reduces the component of slope angle error introduced by ignoring sub-raster topography, the slope angle values calculated from neighboring points will likely have the same magnitude of uncertainty. This result can be understood by considering the Haneberg (2004) analytical approximation for slope angle uncertainty given in equation (4). For the baseline case of zero slope, the slope angle standard deviation given by equation (4) becomes approximately

$$s_\beta = \frac{1}{\sqrt{2}} \frac{180}{\pi} \frac{s_\varepsilon}{\Delta x} \tag{5}$$

Thus, the elevation error must be reduced proportionally to any decrease in DEM grid spacing if the slope angle variance is to remain constant. Inclusion of the elevation values will introduce a dependence on slope angle, as described above, but the fundamental reciprocal relationship between elevation error and DEM grid spacing remains intact. Equation (5) predicts a maximum slope angle standard deviation of 4.7° for the conventional 10 m DEM elevation error data in Haneberg (in review) and 3.3° for the LiDAR data in this paper. Thus, reducing the DEM grid spacing by a factor of 10 reduced the slope angle variance by a factor of only 1.4 in this study area.

ACKNOWLEDGEMENTS

The LiDAR elevation data and metadata used in this study were provided by the Puget Sound LiDAR Consortium.

REFERENCES

Adams, J. and Chandler, J., 2002, Evaluation of lidar and medium scale photogrammetry for detecting soft-cliff coastal change: *Photogrammetric Record*, v. 17, p. 405-418.

Baum, R.L, Savage, W.Z., and Godt, J.W., 2002, *TRIGRS— A Fortran Program for Transient Rainfall Infiltration and Grid-Based Regional Slope-Stability Analysis (Version 1.0)* : U.S. Geological Survey Open-File Report 12-424, 61 p.

Cochrane, T.A. and Flanagan, D.C., 2003, Representative hillslope methods for applying the WEPP model with DEMs and GIS: *Transactions of the American Society of Agricultural Engineers*, v. 46, p. 1041-1049.

Cressie, N. and Hawkins, D.M., 1980, Robust estimation of the variogram: *Mathematical Geology*, v. 12, p. 115-125.

Fisher, P., 1998, Improved modeling of elevation error with geostatistics: *GeoInformatica*, v. 2, p. 215-233.

Goovaerts, P., 1997, *Geostatistics for Natural Resources Evaluation*: Oxford University Press, 483 p.

Guzetti, F., Crosta, G., Detti, R., and Agliardi, F., 2002, STONE: a computer program for the three-dimensional simulation of rock-falls: *Computers & Geosciences*, v. 28, p. 1079-1093.

Haneberg, W.C., in review, Effects of digital elevation model errors on spatially distributed seismic slope stability calculations— an example from Seattle, Washington: *Environmental & Engineering Geosciences*.

Haneberg, W.C., 2004, A rational probabilistic method for spatially distributed landslide hazard assessment: *Environmental & Engineering Geosciences*, v. 10, p. 27-43.

Haneberg, W.C., Creighton, A.L., Medley, E.W., and Jonas, D., 2005, Use of LiDAR to assess slope hazards at the Lihir gold mine, Papua New Guinea: Vancouver, British Columbia, Proceedings of the 2005 International Conference on Landslide Risk Management, May 31 – June 2, 2005 (in press).

Hodgson, M.E. and Bresnahan, P., 2004, Accuracy of airborne lidar-derived elevation: empirical assessment and error budget: *Photogrammetric Engineering & Remote Sensing*, v. 70, no. 2, p. 331-339.

Holmes, K.W., Chadwick, O.A., and Kyriakidis, P.C., 2000, Error in a USGS 30-meter digital elevation model and its impact on terrain modeling: *Journal of Hydrology*, v. 233, p. 154-173.

Isaaks, E.H. and Srivastava, R.M., 1989, *Applied Geostatistics*: Oxford University Press, 561 p.

McKean, J. and Roering, J., in review, Operational accuracy of lidar in mountainous terrain: *Journal of Hydrology*.

McKean, J. and Roering, J., 2004, Objective landslide detection and surface morphology mapping using high-resolution airborne laser altimetry: *Geomorphology*, v. 57, p. 331-351.

Norheim, R.A., Queija, V.R., and Haugerud, R.A., 2002, Comparison of LIDAR and INSAR DEMs with dense ground control, in *Proceedings, 2002 ESRI International User Conference*: San Diego, California, July 8-12, 2002, paper 0442, http://gis.esri.com/library/userconf/proc02/pap0442/p0442.htm (available online only).

Pack, R.T., Tarboton, D.G., and Goodwin, C.N., 1998, *Terrain Stability Mapping with SINMAP, Technical Description and Users Guide for Version 1.00*: Salmon Arm, British Columbia, Terratech Consulting, Ltd., Report Number 4114-0 (report available from http://www.engineering.usu.edu/dtarb).

Pebesma, E.J., 2004, Multivariable geostatistics in S: The gstat package. *Computers & Geosciences*, v. 30, p. 683-691.

Quinn, P., Beven, K., Chevallier, P., and Planchon, O., 1991, The prediction of hillslope flow paths for distributed hydrological modeling using digital terrain models: *Hydrological Processes*, v. 5, p. 59-80.

Shaw, S.C. & Vaugeois, L.M., 1999, *Comparison of GIS-Based Models of Shallow Landsliding for Application to Watershed Management*: Olympia, Washington Department of Natural Resources Report TFW-118.

Sidle, R.C. and Wu, W., 1999, Simulating effects of timber harvesting on the temporal and spatial distribution of shallow landslides: *Zeitschrift für Geomorphologie*, v. 43, p. 77-101.

Tarboton, D. G., 1997, A new method for the determination of flow directions and contributing areas in grid digital elevation models: *Water Resources Research*, v. 33, p. 309-319

Troost, K. G., Booth, D. B., and S. Shimel, in review, Geologic map of the Seattle Southwest quadrangle: U.S. Geological Survey Miscellaneous Investigations Map, scale 1:12,000.

Ward, T.J., Li, R.M., and Simons, D.B., 1981, Use of a mathematical model for estimating potential landslide sites in steep forested drainage basins, *in Erosion and Sediment Transport in Pacific Rim Steeplands*: IAHS Publication 132, p. 21-40.

Zevenbergen, L.W. and Thorne, C.R., 1987, Quantitative analysis of land surface topography: *Earth Surface Processes and Landforms*, v. 12, p. 47-56.

FIGURE CAPTIONS

Figure 1. Index map showing the general location of the study area.

Figure 2. Composite orthophoto and shaded relief image with locations of the static and kinematic stop-and-go GPS data points. UTM Zone 10 N grid ticks are shown along the upper and right margins.

Figure 3. Histograms of clustered (top) and cell-declustered (bottom) elevation errors measured in this study, normalized so that the area under the bars of each histogram sums to unity.

Figure 4. Empirical relationships between the magnitude of the measured elevation error and elevation, slope angle, slope aspect, and topographic roughness.

Figure 5. North-south, east-west, and omnidirectional variograms of the measured elevation errors. Bin width is 250 m and the angular tolerance for the directional variograms is ±22.5°. Solid line in the omnidirectional variogram is the best-fit model variogram obtained by least-squares fitting and described by equation (1).

Figure 6. Results of local kriging estimation and stochastic simulation of the elevation error field across the entire study area based on the model variogram given by equation (1) and a declustered error mean of –0.11 m. A) Kriged elevation errors (local kriging using 100 nearest data points). B) Kriging standard deviation. C-F) Four of the 25 elevation error realizations produced using sequential Gaussian simulation with normal score back transformation. G) Simulated mean elevation error distribution obtained from the 25 stochastic simulations. H) Simulated elevation error standard deviation distribution obtained from the 25 stochastic simulations.

Figure 7. Results of Monte Carlo simulation of the effect of observed elevation errors on slope angles and slope aspects calculated for hypothetical north-facing slopes with true slope angles of 0°, 10°, and 20°. Each of the three simulations consists of 1000 realizations of slope angle and slope aspect.

Figure 8. Calculated slope angle standard deviations as predicted by Monte Carlo simulations from Figure 7 (plus one additional simulation for a true slope angle of 45°) and the first-order, second-moment approximation of Haneberg (2004). Elevation difference refers to the squared sum of the squared row and column elevation differences used in the Zevenbergen and Thorne (1987) finite difference formula for slope angle.

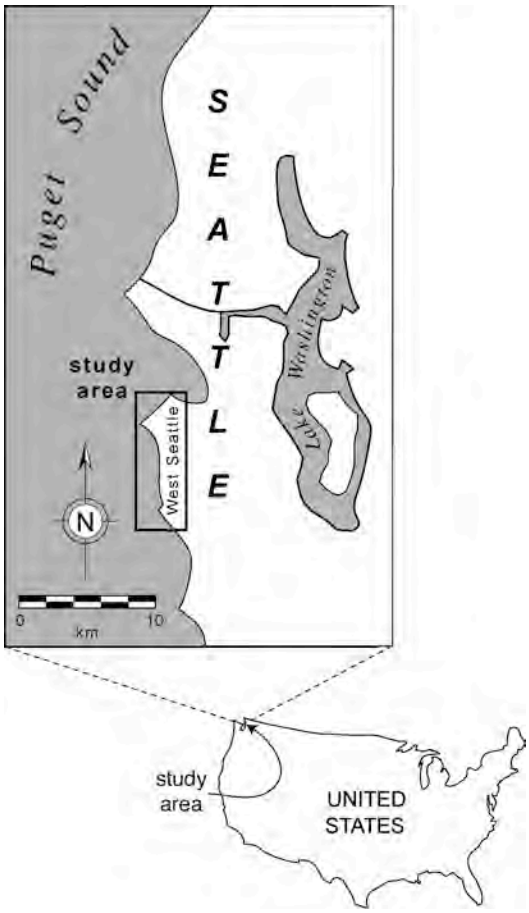
Puget Sound
SEATTLE
Lake Washington
study area
West Seattle
N
0
km
10
study area
UNITED STATES

Figure 1

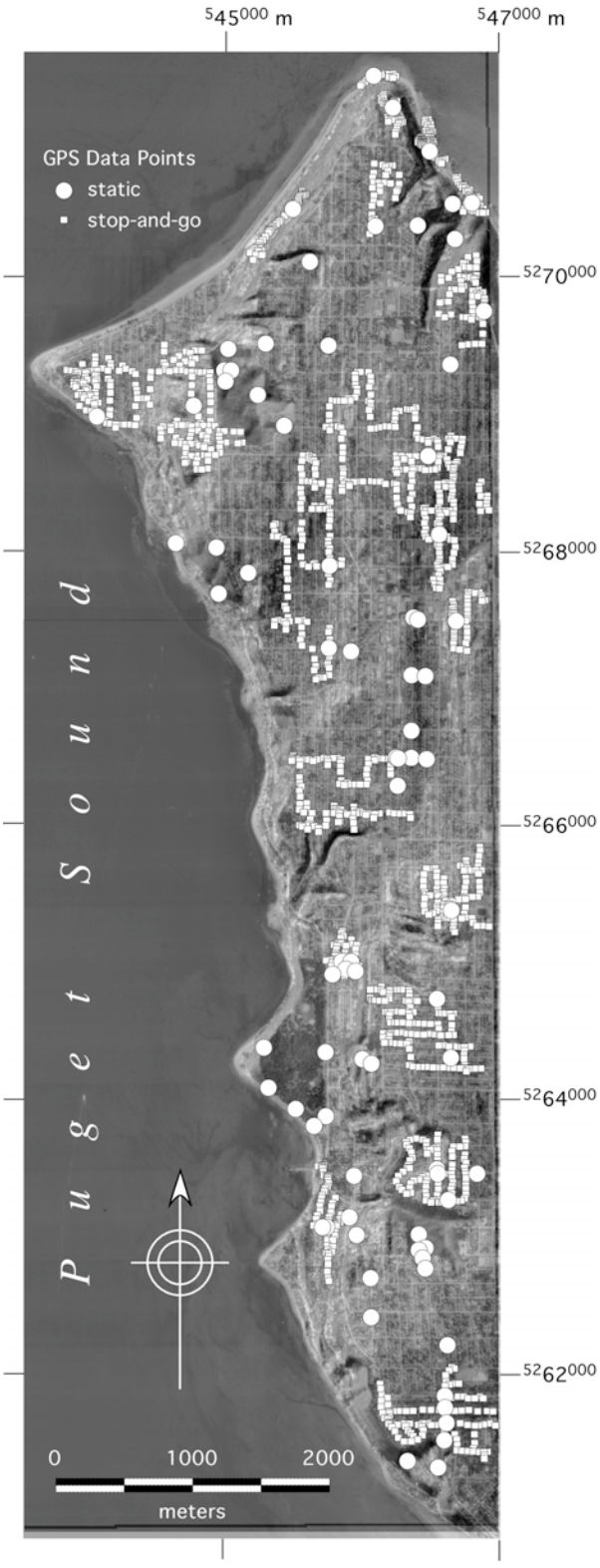
545000 m
547000 m
GPS Data Points
static
stop-and-go
5270000
5268000
5266000
5264000
5262000
Puget Sound
0
1000
2000
meters

Figure 2

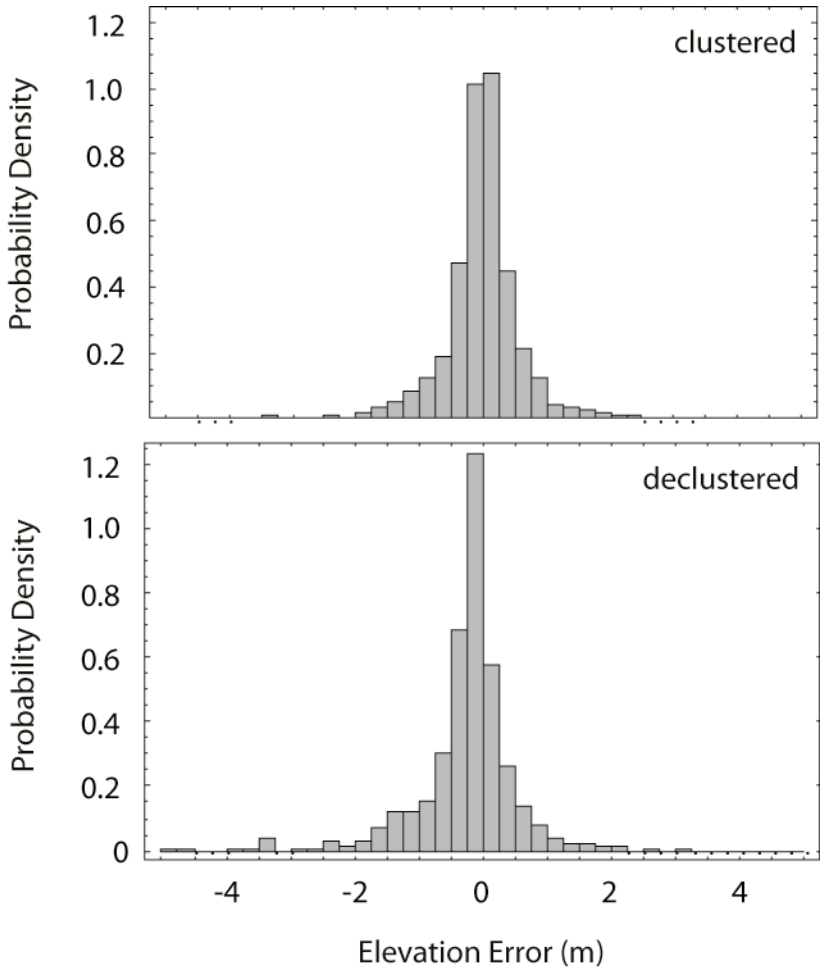
clustered
declustered
Probability Density
Probability Density
1.2
1.0
0.8
0.6
0.4
0.2
0
-4
-2
0
2
4
Elevation Error (m)

Figure 3

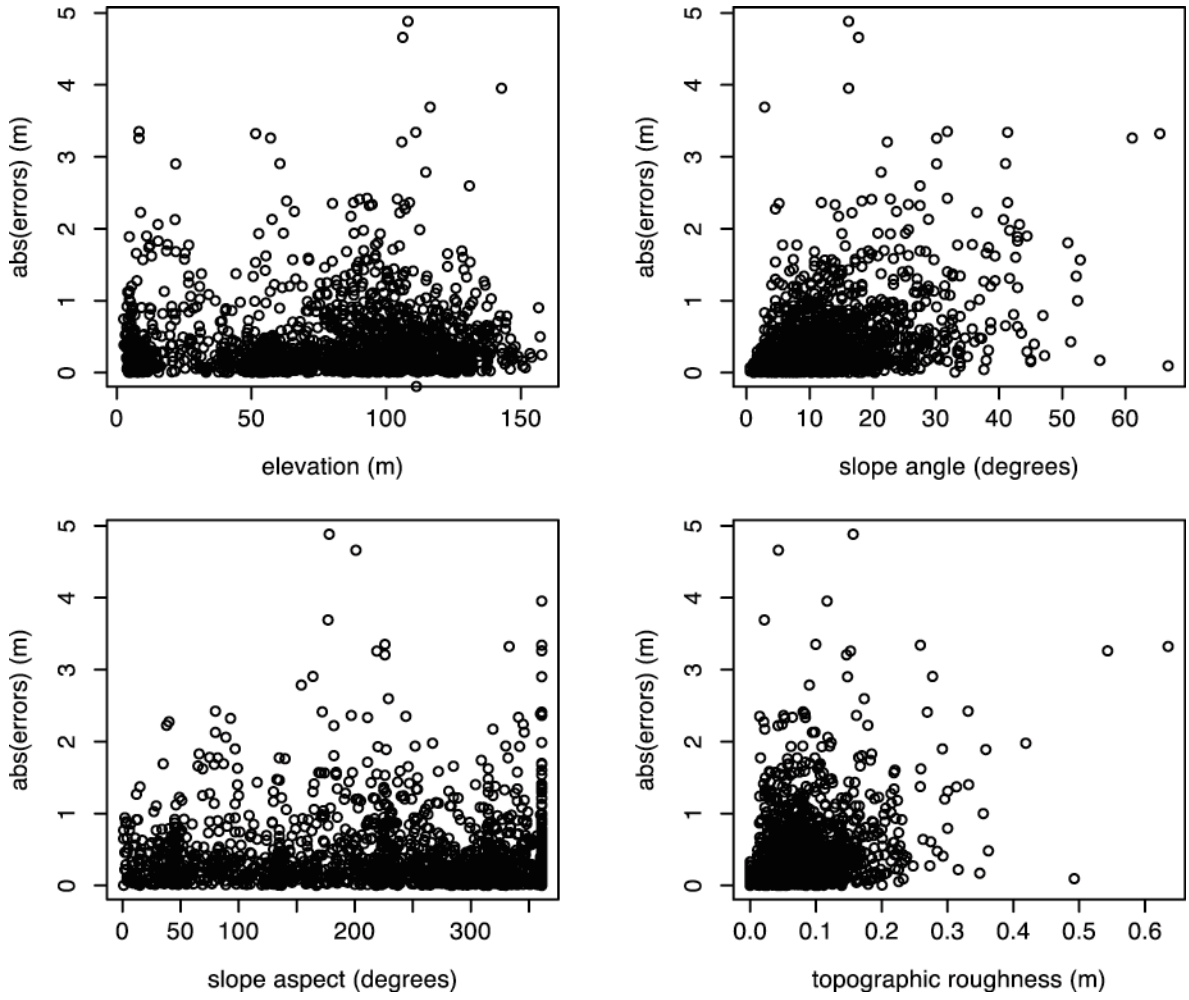
abs(errors) (m)
elevation (m)
slope angle (degrees)
slope aspect (degrees)
topographic roughness (m)

Figure 4

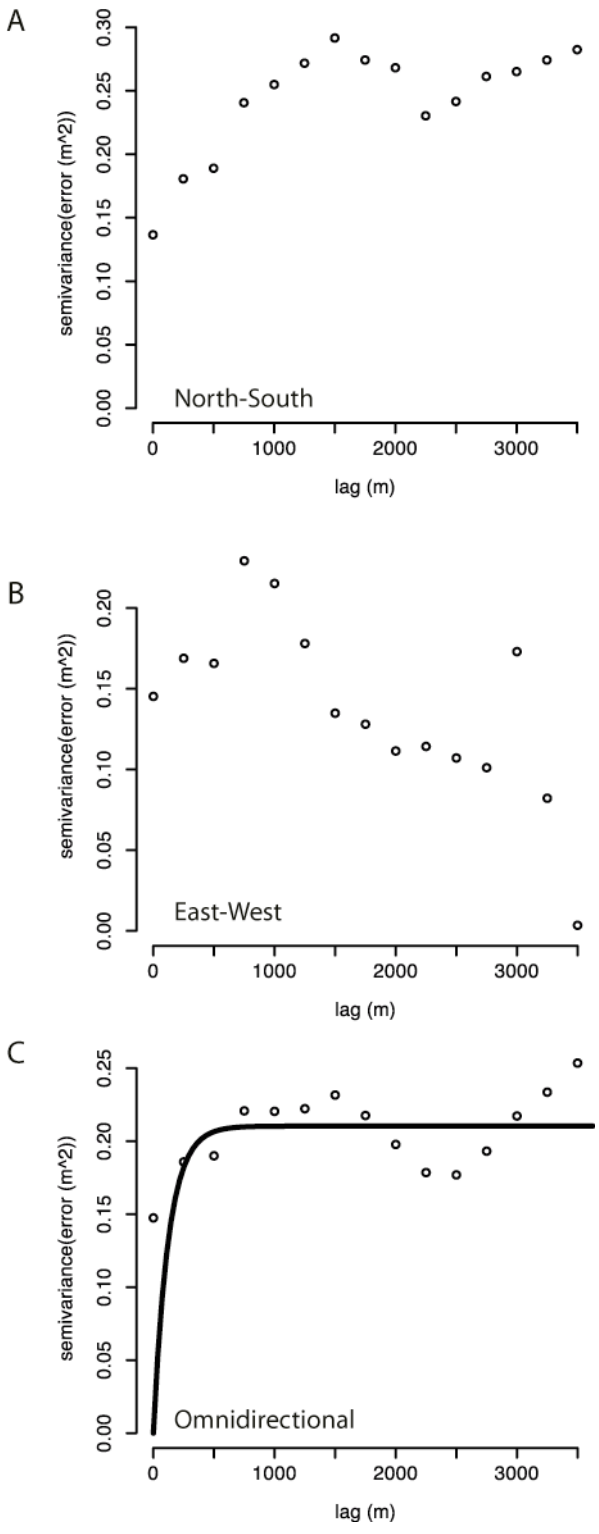
A
semivariance(error (m^2))
0.00
0.05
0.10
0.15
0.20
0.25
0.30
North-South
0
1000
2000
3000
lag (m)
B
semivariance(error (m^2))
0.00
0.05
0.10
0.15
0.20
East-West
0
1000
2000
3000
lag (m)
C
semivariance(error (m^2))
0.00
0.05
0.10
0.15
0.20
0.25
Omnidirectional
0
1000
2000
3000
lag (m)

Figure 5

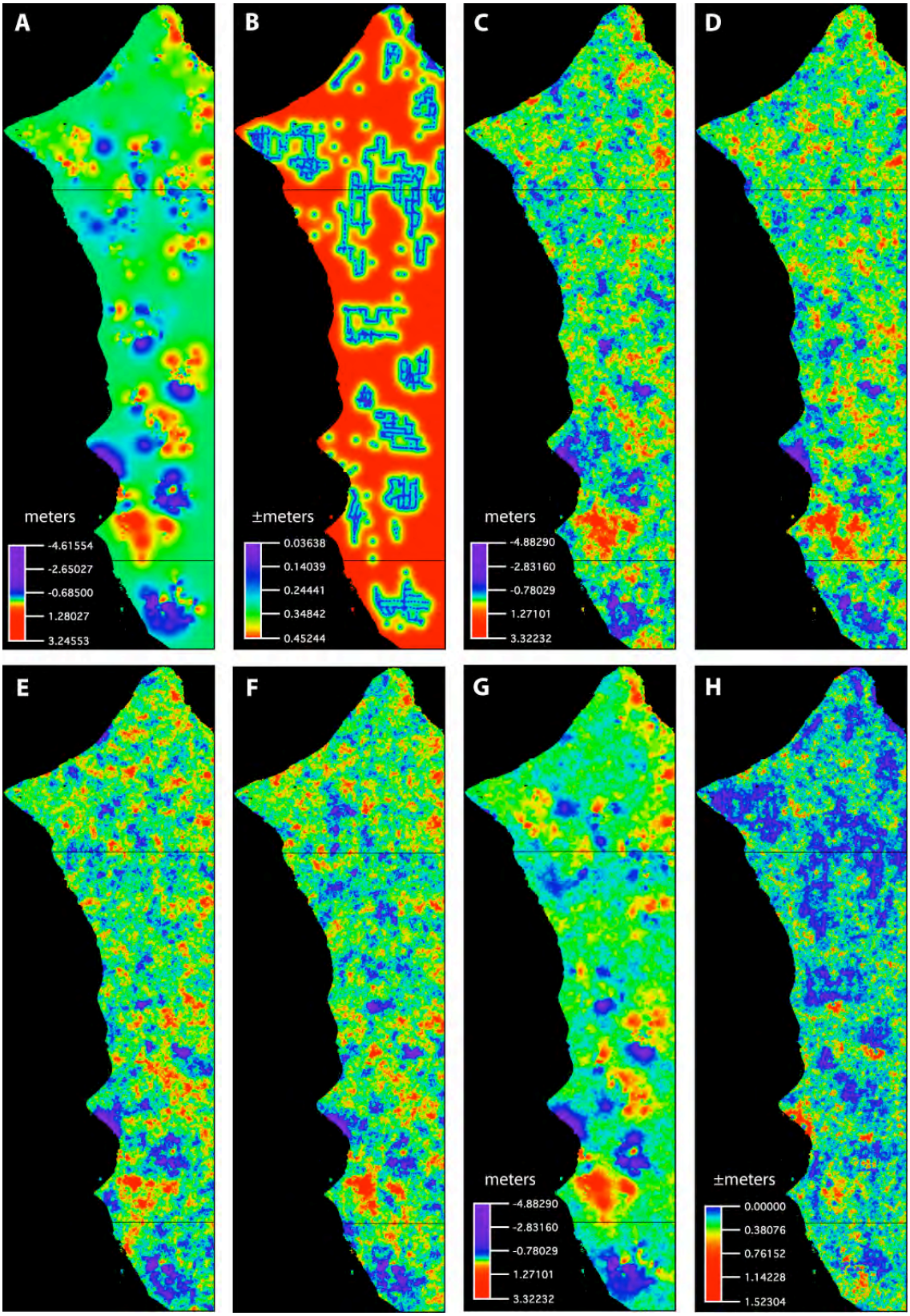
A
meters
-4.61554
-2.65027
-0.68500
1.28027
3.24553
B
±meters
0.03638
0.14039
0.24441
0.34842
0.45244
C
meters
-4.88290
-2.83160
-0.78029
1.27101
3.32232
D
E
F
G
meters
-4.88290
-2.83160
-0.78029
1.27101
3.32232
H
±meters
0.00000
0.38076
0.76152
1.14228
1.52304

Figure 6

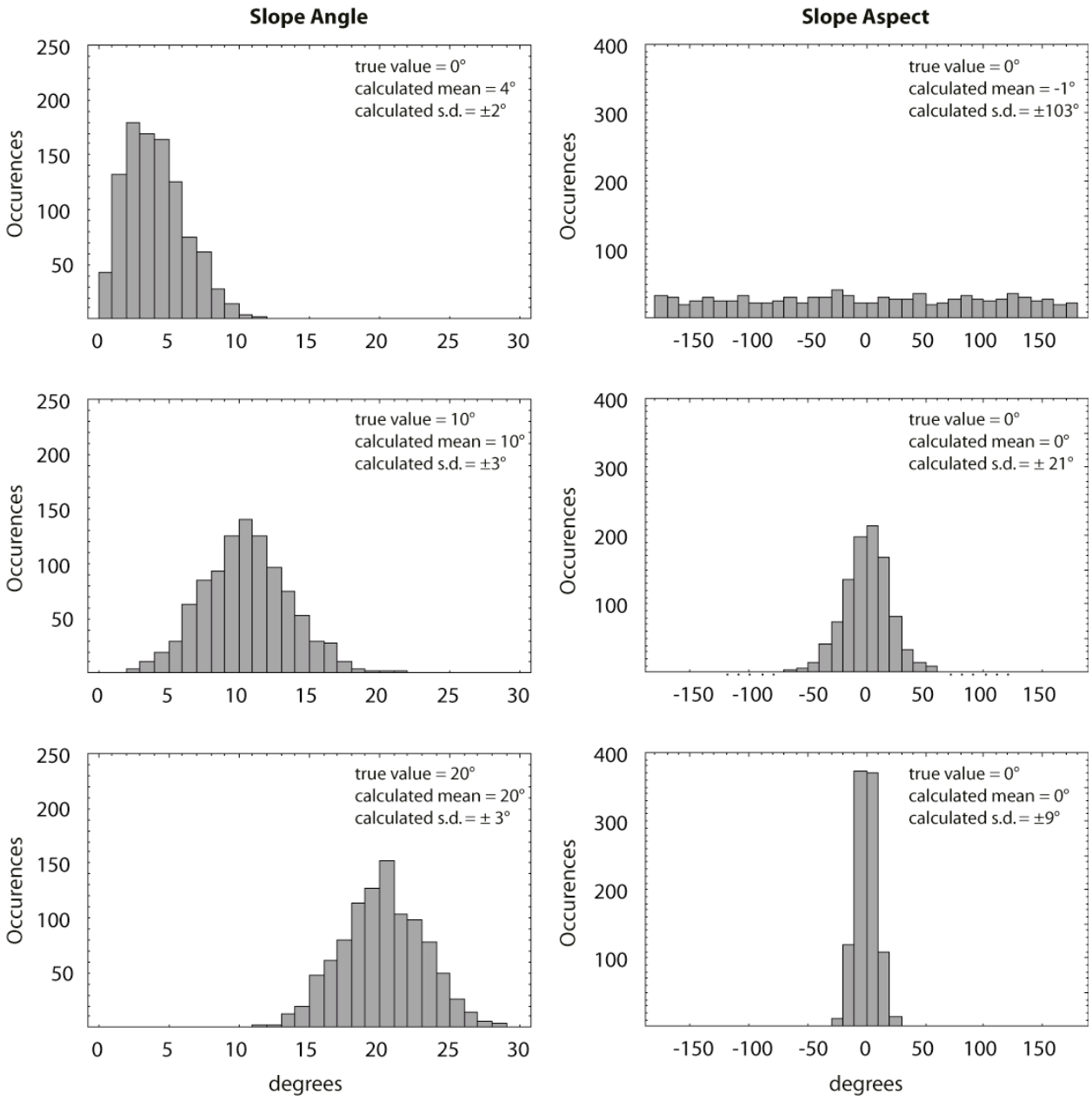
Slope Angle
Slope Aspect
Occurences
true value = 0°
calculated mean = 4°
calculated s.d. = ±2°
true value = 0°
calculated mean = -1°
calculated s.d. = ±103°
true value = 10°
calculated mean = 10°
calculated s.d. = ±3°
true value = 0°
calculated mean = 0°
calculated s.d. = ± 21°
true value = 20°
calculated mean = 20°
calculated s.d. = ± 3°
true value = 0°
calculated mean = 0°
calculated s.d. = ±9°
degrees
degrees

Figure 7

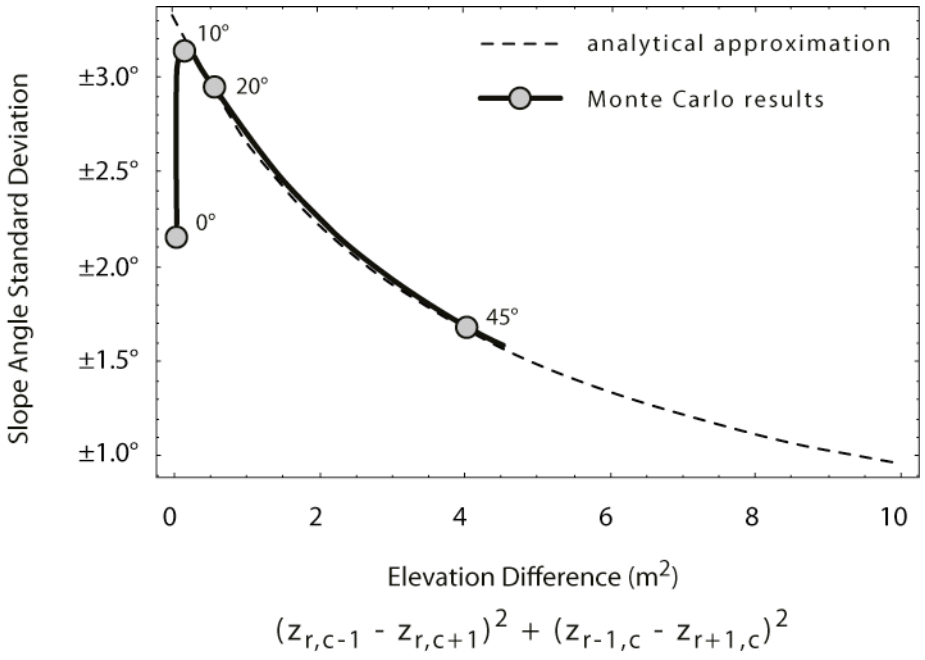
Slope Angle Standard Deviation
±3.0°
±2.5°
±2.0°
±1.5°
±1.0°
10°
20°
0°
45°
analytical approximation
Monte Carlo results
0
2
4
6
8
10
Elevation Difference (m²)
$(z_{r,c-1} - z_{r,c+1})^2 + (z_{r-1,c} - z_{r+1,c})^2$

Figure 8